

4

Frequency Modulated Analog Fiber Optic Links using Direct Detection

by

Jeffrey Matthew Roth

Submitted to the Department of Electrical Engineering and Computer Science
in partial fulfillment of the requirements for the degree of

Master of Engineering in Electrical Engineering and Computer Science

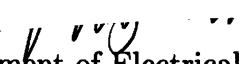
at the

MASSACHUSETTS INSTITUTE OF TECHNOLOGY

May 23, 1997

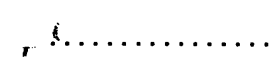
© M.I.T., MCMXCVII. All rights reserved.

Signature of Author


Department of Electrical Engineering and Computer Science

May 23, 1997

Certified by


James K. Roberge

Professor of Electrical Engineering

Thesis Supervisor

Approved by


Charles H. Cox III

Senior Staff Member, MIT Lincoln Laboratory

Technical Supervisor

Accepted by


Arthur C. Smith

Chairman, Department Committee on Graduate Theses

OCT 29 1997

Frequency Modulated Analog Fiber Optic Links using Direct Detection

by

Jeffrey Matthew Roth

Submitted to the Department of Electrical Engineering and Computer Science
on May 23, 1997, in partial fulfillment of the
requirements for the degree of
Master of Engineering in Electrical Engineering and Computer Science

Abstract

The modulation of optical carriers by radio frequency (RF) and microwave signals has proven to be a promising means of fulfilling needs in the analog realms of antenna remoting, common antenna television (CATV), phased array radar element control, and cellular communication links. Among the many techniques used in analog fiber links, intensity modulation has been most widely investigated for both direct and external modulation links. Limitations on noise figure and dynamic range have recently led people to pursue the use of optical frequency modulation (FM) links.

The goal of this thesis is to take advantage of feedback to demodulate an optical FM signal through a electro-optically tuned unbalanced Mach-Zehnder interferometer. The sensitivity of the receiver can be increased by the fixed path length difference introduced in the interferometer, thereby enhancing the gain of the link. Experimental and theoretical analysis of the gain, noise figure, and dynamic range for this direct detection optical FM link will be discussed, and we will compare these figures of merit to those attained with other direct detection links.

Thesis Supervisor: James K. Roberge

Title: MIT Professor of Electrical Engineering

Technical Supervisor: Charles H. Cox III

Title: Senior Staff Member, MIT Lincoln Laboratory

Contents

1	Introduction	14
1.1	Analog Optical Links	15
1.2	Background in Modulation Techniques	16
1.2.1	Intensity Modulation	16
1.2.2	Frequency Modulation	17
1.3	Background in Detection Techniques	17
1.3.1	Direct Detection	17
1.3.2	Coherent Detection	18
1.3.3	FM Detection Methods	20
2	Overview of FM Direct Detection (FMDD) Link	22
2.1	FM Source	22
2.1.1	Linewidth and Phase Noise	25
2.1.2	Spectrum Measurements	25
2.1.3	Tuning Sensitivity and Wavelength Displacement	27
2.2	Demodulator	29
2.2.1	Mach-Zehnder Interferometer (MZI)	30
2.2.2	Dual Photodetector Balanced Receiver	34
2.2.3	Feedback Loop	36
3	Link Modeling	39
3.1	Loop Gain	39
3.1.1	Linearization Method	41
3.1.2	Gain Coefficients	42
3.1.3	Gain and Bandwidth Calculation	42

3.2	Alternative Gain Formulation (Phase Model)	43
3.2.1	Input	46
3.2.2	Feedback loop	47
3.2.3	Interferometric combining and loop filter	47
3.2.4	Gain Result	48
3.3	Dynamic Range	48
3.4	Noise Figure	52
4	Experimental Results and Conclusions	56
4.1	Link Measurements	56
4.1.1	Gain	56
4.1.2	Noise Figure	59
4.1.3	Spurious-Free Dynamic Range	61
4.2	Discussion	61
4.3	Conclusions and Future Work	63
A	Free-Space Source-to-Fiber Design	65
A.1	Background	65
A.2	Collimation	66
A.3	PM Fiber Coupling	66
A.3.1	Beam Expander	68
A.3.2	Improvements	68
B	Free-Space Source Considerations	69
B.1	Link Transmitter	69
B.2	Link Photo	69
C	Feedback Loop Analysis	72
C.1	First order loop	72
C.2	Second order loop overview	72
D	Dual-Detector Balanced Receiver	74
E	MAPLE Scripts	76
E.1	Gain Analysis - Intensity Model	76

E.2	Gain Analysis - Phase Model	77
E.3	Dynamic Range Analysis	78
E.4	Noise Figure Analysis	81
F	List of Abbreviations	84

List of Figures

1-1	Fundamental building blocks of analog fiber optic links.	15
1-2	Link block diagram showing a direct IM (intensity modulation) transmitter plus a direct detection photodetector receiver.	16
1-3	Link block diagram showing external IM transmitter plus photodetector receiver.	17
1-4	Coherent detection system.	19
1-5	Comparison of SFDR for FM coherent detection links and IM direct detection links. Graph is obtained from [14].	20
2-1	Block diagram of FM link using a push-pull YBBM MZI. The output of the two arms of the YBBM give an intensity proportional to $1 \pm \cos(\phi)$, respectively, where ϕ represents the wavelength-dependent and MZI electrode voltage-dependent phase difference between the two arms of the interferometer. The balanced receiver subtracts the two outputs, so that the total photocurrent is proportional to $2\cos(\phi)$	23
2-2	Conceptual diagram of electro-optically tunable solid state laser. The pump radiation at 808 nm is incident from the left, and the device lases at 1.064 μm and transmits in the direction of the positive optic axis. The right edge of the LiTaO ₃ crystal is mirror coated for transmittance at 1.064 μm and reflectance at 808 nm. Lead and copper are used to dampen low frequency vibrational modes.	24
2-3	Calculated transfer characteristics for electro-optically tunable laser. Wavelength versus voltage tuning sensitivity $\eta \approx 5.7 \times 10^{-14}$ nm/V (or 15 MHz/V) over a 1 GHz bandwidth centered 282 THz (1.064 μm).	24

2-4	Measurement of tunable Nd:YAG laser spectrum using SuperCavity scanning Fabry-Perot. Horizontal axis N represents optical frequency normalized to free-spectral range (FSR) of cavity and referenced to center wavelength ($\nu_o = 282.000$ THz): $N \triangleq \frac{400}{\text{FSR}}(\nu - \nu_o)$. FSR of cavity is 3 GHz, with plot spanning 1.25 FSRs. Laser's FSR is about 90 GHz, so numerous spikes are either due to convolved (<i>i.e.</i> , nonadjacent) multimode behavior, or more likely, improper mode-matching to the SuperCavity. We measure each peak to have FWHM ~ 1 MHz.	26
2-5	Block diagram of FM link using standard MZI. The optical attenuation is set to -3 dB, scaled by the fiber-to-fiber MZI insertion loss, t_{ff}	30
2-6	Mach-Zehnder Interferometer intensity versus electrode voltage (defined in our link as V_{out}) transfer function shown in (2.18). It is assumed that $\Delta\ell = 0$ so that the transfer function has no phase offset under zero voltage. Also $\lambda \rightarrow \lambda_o$. V_π is shown as the switching voltage or voltage that swings the phase by π . The linear (-3 dB) operating point is shown also. Arbitrary units are shown on both axes.	32
2-7	Mach-Zehnder Interferometer intensity versus optical frequency transfer function, assuming zero phase difference at zero $\Delta\nu$. The peak-to-null spacing $\Delta\nu$ is related to $\Delta\ell$ by (2.11). Arbitrary units are shown on both axes.	34
2-8	Measurement of maximum $\Delta\ell$ in modulator given a broadband optical noise source. For this half-coupler modulator the transfer characteristic is a sum of sinusoids, so alternating hump behavior results. Global maxima exist when the phase difference across the two arms $\phi = m\pi$ and local maxima exist when $\phi = \frac{2m+1}{2}\pi$, ($m = 1, 2, \dots$). The Gaussian-like envelope is due to the spectral characteristics of the source.	35
2-9	Mach-Zehnder Interferometer constructed out of PM optical fiber, 3 dB couplers, and EO phase modulator. Fixed changes in $\Delta\ell$ are accomplished with a PM fusion splicer.	35

2-10	Major circuit components of first-order integrating FM demodulator. Most of the amplifiers shown are standard Op Amps. The dual photodetector receiver is shown with bias capacitors to allow RF paths to ground while applying reverse bias voltages to the photodetectors; the photodetector midpoint is maintained at a virtual ground due to the negative input characteristics of the Op Amp. The non-inverting buffer amplifier converts current i_f to voltage.	37
2-11	Detailed schematic of FM link including feedback electronics.	38
3-1	Explicit FM demodulator gain block diagram showing small signal model relationships for Intensity Model.	40
3-2	Three dimensional bode plot of power gain (dB) versus $\log_{10}(\frac{\Delta\ell}{1\text{m}})$ for FM link. Path length difference axis is labelled by $M \triangleq \log_{10}(\frac{\Delta\ell}{1\text{m}})$. Frequency axis is labeled by $N \triangleq \log_{10}(\frac{\omega}{1\text{rad/sec}})$. Below breakpoint frequency, gain is a flat -46 dB with ~ 1 m of path length difference; after breakpoint frequency response falls of at -20 dB/dec. Plot shown for V_o of 2.5 V, V_π of 5.0 V, and \mathcal{R} of .4 A/W. P_{in} is 4 mW and t_{ff} set to 0.25. See Table 3-1 for other parameters.	44
3-3	Intensity Model Gain in dB plotted versus $\log_{10}(\frac{\Delta\ell}{1\text{m}})$ at a fixed frequency 1 MHz. This plot is a two-dimensional slice of Figure 3-2.	45
3-4	Intensity Model Gain in dB versus $\log_{10}(\frac{\omega}{1\text{rad/sec}})$ at a fixed path length difference $\Delta\ell = 1.080$ m. The model shows a -3 dB breakpoint of 20 MHz. This plot is a two-dimensional slice of Figure 3-2.	45
3-5	Small-signal FM link demodulator gain block diagram using Phase Model. .	46
3-6	Noise floor (dBm) plotted versus $\log_{10} \Delta\ell$ at 1 MHz using given link parameters.	52
3-7	Spurious Free Dynamic Range (dB \times Hz $^{2/3}$) plotted versus $n = \frac{\Delta\ell}{1.064\text{ cm}}$ varying from 1 to 100, or .01064 m to 1.064 m. The horizontal $\Delta\ell$ axis is plotted linearly. This plot exaggerates SFDR variation over given range; note vertical axis labels.	53
3-8	Spurious Free Dynamic Range (dB \times Hz $^{2/3}$) plotted versus $n = \frac{\Delta\ell}{1.064\text{ m}}$ varying from 1 to 100, or 1.064 m to 106.4 m. The horizontal $\Delta\ell$ axis is plotted linearly.	53
3-9	Noise figure (dB) model plotted versus $\log_{10} \Delta\ell$ (referenced to 1 m) using parameters in Table 3-1. Plotted at 1 MHz.	54

3-10	FMDD noise figure model and modified Cox noise figure model in [26] plotted together versus $\log_{10} \Delta\ell$ (referenced to 1 m) using parameters in Table 3-1. FMDD model represented with o-marks, while modified noise figure model of Cox represented by x-marks. The models agree perfectly with both showing noise figure improvements with increasing $\Delta\ell$. Plot shown for 1 MHz. . . .	55
4-1	Experimental comparison of FMDD gain model and experimental result. The gain in dB is plotted versus $\log_{10}(\frac{\omega}{1\text{rad/sec}})$ at $\Delta\ell = 1$ m. The lower trace is the experimental result at $\Delta\ell = 1.080$ m, while the upper trace is the result previously shown in Figure 3-7. Results agree to within 5 dB at frequencies below the experimental 3 dB breakpoint of $f_{3dB} = 6.4$ MHz. The model f_{3dB} occurs at 20 MHz.	57
4-2	Experimental verification of Intensity Model. The gain in dB is plotted versus $\log_{10}(\frac{\omega}{1\text{rad/sec}})$ at $\Delta\ell = 1$ m. The upper trace is the experimental result at $\Delta\ell = 1.080$ m, while the lower trace is the result previously shown in Figure 3-4. Results agree to within 0.5 dB at frequencies below the experimental 3 dB breakpoint of $f_{3dB} = 6.4$ MHz. The model f_{3dB} occurs at 20 MHz. Lower breakpoint and faster rolloff observed in the data are believed to be due to the unmodeled characteristics of the Op Amps.	58
4-3	Link gain measurement. Time domain response at 1 MHz. The lower trace is the link output at 20 mV peak-to-peak and the upper trace is the link input at 2 V peak-to-peak. The gain in dB is $20 \log_{10}(\frac{20\text{mV}}{2\text{V}}) = -40$ dB.	59
4-4	Comparison of adjusted noise figure model and experimental result at 1 MHz. The parameters η and V_{π} were adjusted. The noise figure in dB is plotted versus $\log_{10}(\frac{\Delta\ell}{1\text{m}})$. Our experimental yielded $\text{NF} = 40$ dB at $\Delta\ell = 1.080$ m, while the model gives 45.0 dB. Discrepancy of 5 dB is likely due to measurement error and modeling.	60
4-5	Link input spectrum at 1 MHz, viewed over 50 kHz band. Input is 9 dBm measured under 50Ω load of RF spectrum analyzer. Normal load is $\sim 1 \text{M}\Omega$. Noise floor is -93 dBm over a 1 Hz bandwidth. Measurement yields $\text{SNR}_{in} = 102$ dB.	60

4-6	Link output spectrum at 1 MHz, viewed over 50 kHz band. Output is at -71 dBm under 50 Ω RF spectrum analyzer load; V_{out} is attenuated by .068 through a resistor before being sent to spectrum analyzer low impedance input. Noise floor is -133 dBm over a 1 Hz bandwidth. Measurement yields $SNR_{out} = 62$ dB.	61
A-1	Free-space beam collimation setup using single plano-convex lens.	66
A-2	Waist size in meters for $f = 20$ cm lens.	67
A-3	Waist size in meters for $f = 20$ cm lens and $l = 21$ cm lens position.	67
A-4	Free-space beam expander setup using single plano-convex lenses.	68
B-1	Free-space optical transmitter for FMDD link.	70
B-2	Photo of free-space portion of optical FMDD link including the 3dB coupler and phase modulator of the fiber-based receiver.	71
C-1	Second-Order Integrator.	73
C-2	Second-Order Integrator Bode Plot with $C_1 = 100$ pF, $C_2 = 1000$ pF, $R_1 = R_2 = 100 \Omega$	73
D-1	Drawing of dual-detector balanced receiver assembly.	74
D-2	Schematic of dual-detector balanced receiver circuit. Detectors are Epitaxx ETX300T InGaAs Photodetectors.	75

List of Tables

- 3.1 Table of link parameter numerical values. 51
- 4.1 Table of free parameter adjustments. 57
- 4.2 Comparison of FMDD link results to the best IMDD links. 62

Acknowledgments

These five years of undergraduate and graduate studies at MIT have gone by quickly, and I will likely soon forget about all those who played such important roles in making my time here both enjoyable and successful. For that reason I would like to recognize these people in writing so I will remember it when I look back on this.

There are many people whom deserve acknowledgment for providing me with help and guidance on my thesis project. I give much thanks to my advisor at Lincoln Lab, Charlie Cox, who has allowed me the privilege to work in his lab since the summer of my junior year. Charlie has always listened to my questions and comments and I have learned a lot from our discussions in his office. My other advisor Ed Ackerman has been pivotal in my thesis project. Ed's deep knowledge of analog optical links gave me extensive guidance in understanding the details of my research; without his help I would not have been able to bring this project to fruition. I thank Prof. Roberge for patiently helping me out with the feedback issues of my work, even though I made the mistake of not taking 6.302. He was very helpful in all aspects of the analog circuit design in my loop filter. I also thank Dave Kettner, the group leader of Group 103 for supporting me and giving me advice about my future.

Within the Group 103 Photonics Team there are many others that have helped me out in various ways. Harold Roussel has always been willing to help me with laboratory tasks. His practical knowledge is impressive and I consider him a real engineer. Allen Yee has been a great friend, and has taught me a lot about measurement techniques for RF systems. I have always enjoyed exchanging MIT stories with him, or talking about famous hacks. Roger Helkey has been a great person to be around since he is always helpful and friendly when I have questions or need to borrow equipment. Roger provided a lot of guidance in helping me successfully build my dual-photodetector receiver. I have enjoyed being around John Vivilecchia in the photonics lab, since he always has a friendly attitude to share with others. He amused myself and others many times by doing excellent re-enactments of various movies. Mike Taylor has been a companion to me in the photonics lab over this past year. It has been fun sitting in front of the J-137b windows discussing issues of life and observing nice days together. Gil Rezendes deserves much recognition since he could always answer questions dealing with RF equipment or circuits. I have missed him since his retirement. Bob Knowlton has been helpful with logistics in getting me organized and set up with my own lab space. I am thankful for his guidance about the procedures and policies at Lincoln. Joelle Prince has always been helpful and encouraging. I am thankful for the numerous times she let me use her computer so that I could finish this thesis. Jane Daneu is a fantastic group secretary, and has been friendly and helpful towards me.

I thank my friend Kohichi Tamura for his inspiration and leadership throughout my years at MIT. He will always be a roll model for me. My parents and brothers, Erich and Chris, deserve much recognition for standing by my side and helping me through the challenges MIT has dealt me. I thank God daily for being blessed with such a wonderful family. This graduate year at MIT has been an exciting year, and I am grateful for the friendships which have developed. My roommate Marc Carlin has become a great friend, and I hope that I might someday learn to be as generous as he is in giving of himself to others. He has become a great model for me and I know that he will be the same for many others as he enters the Navy. I am grateful to the members of my Bible study this year: Christian Trott, Philip Soo, Mike Perrott, Eric Nelson, and Chris Putnam. I am thankful

to God for Park Street Church and for Campus Crusade for Christ, and the friends and fellowship in Boston that these ministries have provided. Despite public conception Boston is a mecca for Christian fellowship, and it is a joy to see how God unites students across these college campuses. A model of this is my friend Kurt Leafstrand who has imparted me with a sliver of his vast knowledge. The times I have spent with him have expanded my mind greatly. I am also thankful for Jennifer Zhou, who has been a great pal and sister in Christ. I thank all the people in Crusade and elsewhere who will be supporting me in Tashkent, Uzbekistan this summer.

I am grateful for my Kwaj memories, and the many friends who I have remained close to during my time at MIT. Thanks to my best friends Paul and Mike, the only two guys that really understand me. Thanks to Amber Shields for always inspiring me and giving me a reason to “dare to dance the rapids”. There are many other friends from Kwaj whom I share a special bond with.

I hope to be able to someday give back to all those who have helped me through my academic pursuits at MIT. If I cannot repay them specifically, may I always remember to share their benevolent attitudes with others.

As I move on to the next phase of life, may I remember the importance of humbleness in following Jesus Christ.

*He has showed you, O man, what is good.
And what does the Lord require of you?
To act justly and to love mercy
and to walk humbly with your God.
-Micah 6:8*

Chapter 1

Introduction

The general purpose of modulation is to exploit the properties of a high frequency carrier signal in order to more efficiently transmit a lower frequency signal between two locations separated by either a long distance or a lossy medium. In optical modulation, an optical cw beam serves as the carrier signal and is modulated with a signal considerably lower in frequency. The modulated signal is transmitted over fiber. The enormous bandwidth of this operation makes it theoretically possible to transmit signals 100's of GHz in bandwidth, something only achievable in millimeter waveguide or a perfectly lossless medium.

Analog optical links have found use in many applications. They are used heavily for remoting RF signals to and from radars and sensors. The lightweight and robust nature of fiber makes optical links suitable for weapons systems aboard planes where transport of high frequency signals is needed. Furthermore, analog optical links allow for concealed and jamming-free transmission of RF signals conventionally transmitted through the atmosphere. Phased array radar antenna dipoles use electro-optic modulators to coherently mix RF signals. Optical links are being found in a growing number of commercial applications. CATV, for example, currently uses fiber links to "broadcast" TV signals to local hubs. Cellular telephone companies connect relay stations with high frequency links that can retransmit the 900 and 1800 MHz communications signals.

Before these growing communications needs can be adequately satisfied, however, analog optical links must be more extensively investigated to improve on their performance and reliability. Since analog optical links are a relatively new field, they are somewhat lacking compared to their digital counterparts. While ultrafast digital optical communications

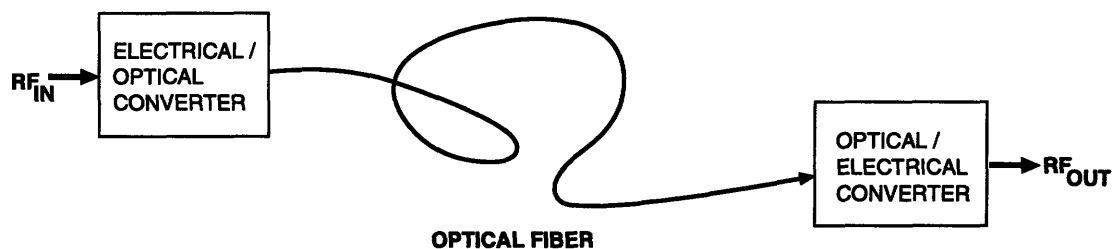


Figure 1-1: Fundamental building blocks of analog fiber optic links.

systems have been proven to work at ≥ 40 Gb/sec [1], there is considerable room for improvement in analog optical links that achieve high performance transmission over similar bandwidths.

The applications for analog links listed above all currently use intensity modulation with direct detection (IMDD). The purpose of this work is to contribute to the research in optical FM receivers for analog fiber optic links. In this thesis a novel approach to FM demodulation is presented that avoids the use of optical heterodyning in the receiver. An optical link is experimentally demonstrated using an in-house high bandwidth electro-optically FM tunable laser source that is detected using a simple interferometric direct detection feedback controlled receiver. The interferometer has an adjustable physical path length difference, denoted $\Delta\ell$, that can vary the sensitivity of the receiver. This system could potentially surpass the performance limitations on gain, dynamic range, and noise figure that are present in most other IMDD links.

1.1 Analog Optical Links

The basic concept of an analog optical link is demonstrated in Figure 1-1. An RF signal is modulated onto an optical carrier via an electrical/optical converter, and the modulated optical signal is transmitted over optical fiber. The receiver is composed of an optical/electrical converter which recovers the original RF signal. Currently the only bandwidth limitations are those imposed by the electrical/optical and optical/electrical converters. In addition to high bandwidth, analog optical links have the important advantage of greatly minimizing interference and loss.

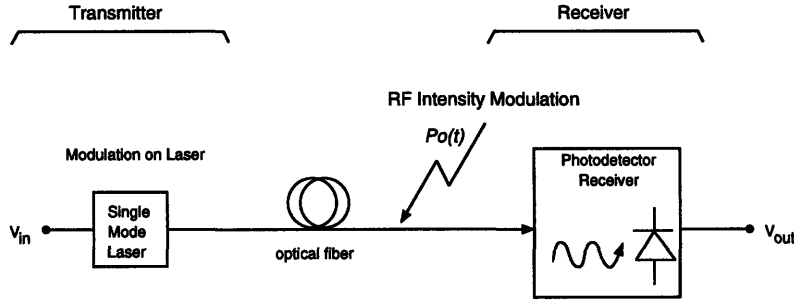


Figure 1-2: Link block diagram showing a direct IM (intensity modulation) transmitter plus a direct detection photodetector receiver.

1.2 Background in Modulation Techniques

1.2.1 Intensity Modulation

Conventional intensity modulated (IM) links are classified as either direct (see Figure 1-2) or external (see Figure 1-3) modulation links.[2] In direct modulation, the output intensity of an optical source, almost always a semiconductor laser¹, is varied by modulating the drive current or voltage with an RF signal. In external modulation, a cw optical beam is intensity modulated by coupling a laser's output into an interferometric device with a voltage-controlled path length difference. The most common type of interferometric external modulator is the electro-optic Mach-Zehnder interferometer in LiNbO₃, although some Mach-Zehnders have been built in polymers [5, 6], and another type of modulator uses an electroabsorption technique [7].

We make an important distinction by referring to these modulation techniques as intensity modulation (IM), rather than amplitude modulation (AM). For IM transmitters, the RF input signal, $V_{in} \cos(\omega_s t)$, is proportional to the modulus-squared of the laser's electric field amplitude, $E(t)$.

$$V_{in} \cos(\omega_s t) \propto |E_s(t)|^2 \quad (1.1)$$

The significance of (1.1) in the overall link behavior will become evident in Section 1.3.1.

¹Pump power modulation techniques using solid-state lasers have also been investigated in [3, 4].

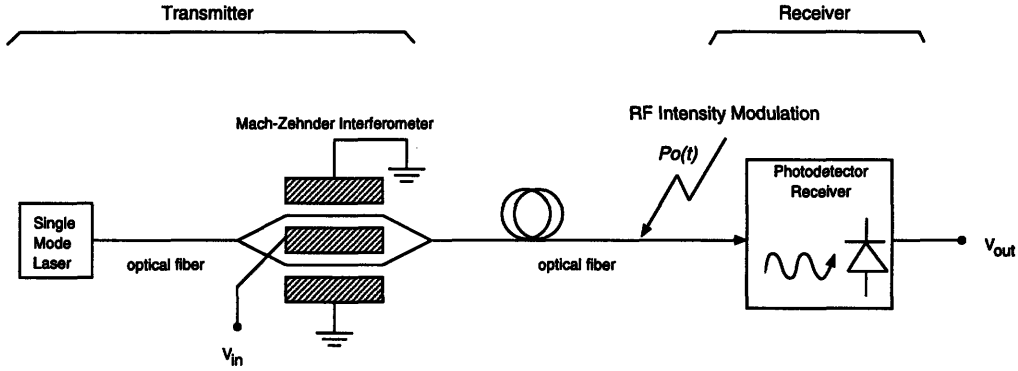


Figure 1-3: Link block diagram showing external IM transmitter plus photodetector receiver.

1.2.2 Frequency Modulation

Frequency modulation (FM) is a more recently explored field of analog fiber optic links. In optical FM the amplitude and frequency of an RF signal are mapped to a singlemode optical signal's frequency deviation amplitude and deviation frequency, respectively. Optical FM has been implemented on a single mode laser cavity in several ways, such as thermal or current tuning, pump-diode modulation [8], piezoelectric tuning [9, 10]. The method used for this work is electro-optic tuning [11, 12] because it shows the most promise and it has attained the highest modulation frequencies yet to date [12].

1.3 Background in Detection Techniques

1.3.1 Direct Detection

Figures 1-2 and 1-3 both show a demodulation technique that retrieves the RF signal from an optical carrier using a single photodetector. This common demodulation technique is called direct detection (DD), since it directly regenerates the original RF signal from the photocurrent produced by incident IM light.

Direct detection is a square-law process, so it can only measure optical intensity, the squared magnitude of a photon's electric field. At the receiver the intensity of an optical signal with optical frequency ω_o and phase ϕ_o is given by

$$P_{out}(t) = \frac{1}{2}n \left| E_s(t) e^{j(\omega_o t + \phi_o)} \right|^2, \quad (1.2)$$

where n is the optical index. The quantity $E_s(t)$ contains modulation information according to (1.1).

The current at the DD receiver is related to the incident intensity through the detector's responsivity, \mathcal{R} , a measure of the amount of photocurrent produced per unit of input optical intensity. It follows from (1.2) that when P_{out} strikes the photodetector, the resulting current i_{out} can be expressed as

$$i_{out}(t) = \mathcal{R}P_{out}(t) \quad (1.3)$$

$$= \frac{1}{2}n\mathcal{R}|E_s(t)|^2. \quad (1.4)$$

Therefore the overall process is linear since (1.1) and (1.4) yield the linear relationship

$$V_{out}(t) \propto i_{out}(t) \propto V_{in} \cos(\omega_s t). \quad (1.5)$$

Note that the direct detection process discards the optical phase, ϕ_o , implying that direct detection is used when optical phase detection is necessary.

The simplicity of direct detection makes it attractive for use in practically all direct and external IM links. The main drawback of direct detection, however, is susceptibility to intensity noise.[13] This limits noise figure (NF) and spurious-free dynamic range (SFDR), two important figures of merit for analog optical links. As shown in [14, 15] it is possible to overcome this limitation by using high optical power (>20 dBm), but this is usually an expensive and therefore undesirable choice in many applications. The link developed in this research combines direct detection with frequency modulation and intensity noise canceling. Such FMDD links could provide improved NF and SFDR at optical powers near 0 dBm, however this experimental work identifies some limitations which must be overcome.

1.3.2 Coherent Detection

To measure optical phase, as well as optical intensity, one usually resorts to coherent detection. Coherent detection is different from direct detection in that it heterodynes a local oscillator, E_{lo} , with the incoming optical signal, E_s , at the photodetector as Figure 1-4 illustrates.

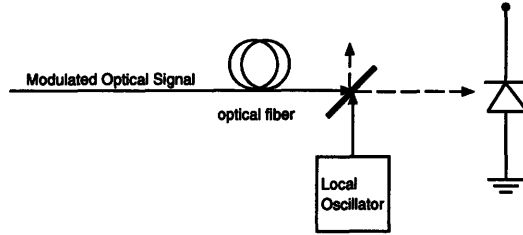


Figure 1-4: Coherent detection system.

To understand this process we start with the intensity expression for $P_{out}(t)$ in (1.6).

$$P_{out}(t) = \frac{1}{2}n|E_{total}(t)|^2 \quad (1.6)$$

The total electric field at the detector is the sum of the local oscillator and received signal fields. The output power becomes

$$P_{out}(t) = \frac{1}{2} \left| E_{lo}e^{j\omega_{lo}t} + E_s(t)e^{j(\omega_s t + \phi_o)} \right|^2. \quad (1.7)$$

The complex exponentials in (1.7) are manipulated to give the (1.8).

$$P_{out}(t) = \frac{1}{2}(|E_{lo}|^2 + |E_s(t)|^2) + E_{lo}E_s(t) \cos((\omega_s - \omega_{lo})t + \phi_o) \quad (1.8)$$

The resultant intensity expression (1.8) contains a low frequency term² and a cosine term at the difference frequency $(\omega_s - \omega_{lo})$. If the LO and signal are closely matched their difference frequency will be within the bandwidth of the detector. Depending upon the application, the quantity (1.8) can be used to measure the signal intensity $|E_s(t)|^2$ or the optical frequency and phase.

While direct detection can only detect intensity of the optical field, coherent detection has the advantage that the phase of the optical signal is preserved. This feature allows coherent detection to be used for detecting frequency modulation. If intensity noise dominates over phase noise, which has been neglected in (1.8), then excellent signal to noise ratio (SNR) can be achieved in an FM system using coherent detection. Even if this is not the case, it has been shown in [16] that coherent detection may be able to achieve phase

²For an FM system with no residual IM it is exactly DC.

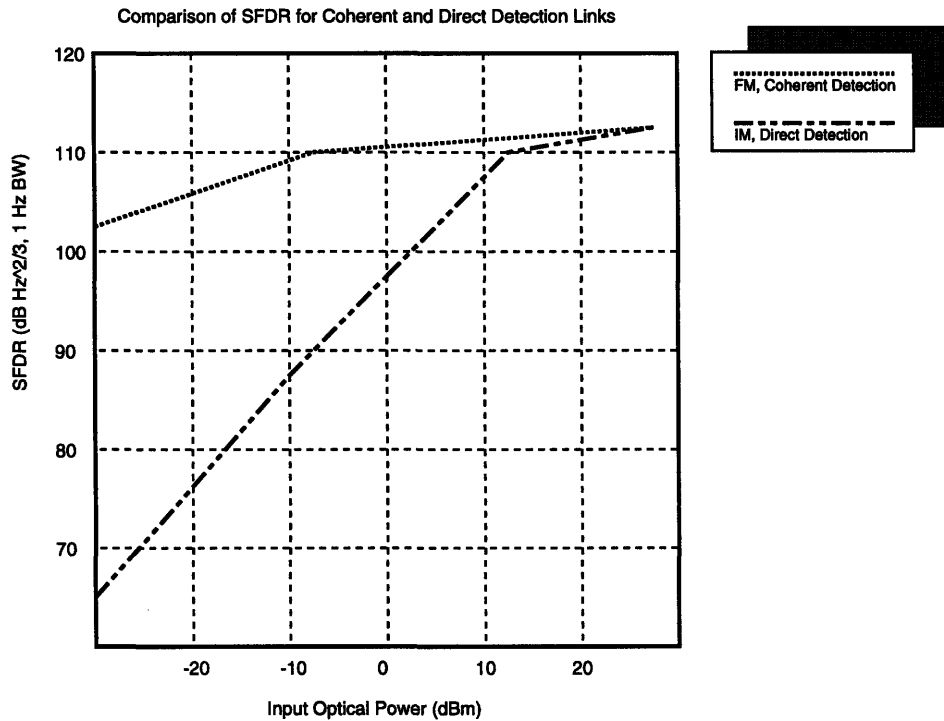


Figure 1-5: Comparison of SFDR for FM coherent detection links and IM direct detection links. Graph is obtained from [14].

noise cancellation. The reason for improved behavior for coherent detection in FM systems is that if good heterodyne efficiency exists (*i.e.*, proper spatial and polarization alignment of LO and signal fields and a high degree of coherence), then the SNR becomes limited only by quantum shot noise.[17]

Kalman, Fan, and Kazovsky have shown that with coherent detection, frequency and phase modulation (PM) can achieve the highest spurious-free dynamic ranges at the lowest optical powers when using a solid-state Nd:YAG laser[14], as Figure 1-5 indicates. Direct detection IM links using either external or direct modulation do not attain SFDR comparable to that of FM/PM systems until about 20 dBm (100 mW) of optical transmitter power.

1.3.3 FM Detection Methods

For links that employ frequency modulation (FM) as the method of modulating the optical carrier, phase information must usually be present at the receiver in order to demodulate

the signal. Such is the case, for example, in the optical phase locked loop design developed by several authors[18, 19] in which a tunable local oscillator is synchronized to the incoming signal light through an integrator feedback loop and the optical equivalent of an XOR gate. As a result of the need for phase information in this and other FM links, coherent detection is the natural choice for demodulating the input signal from the modulated light.

There have recently been several investigations into the use of coherent detection for demodulating optical FM. Kalman et al. have proposed FM and PM links using coherent detection and filtering the photocurrent after it has passed through a frequency or phase discriminator.[14] Sabido et al. have further extended the ideas of frequency modulation as well as intensity modulation in coherent detection systems, and they have provided experimental results for improved dynamic range and SNR using their FM limiter/discriminator receiver design.[20]

Coherent detection feedback loops, termed optical phase-locked loops (OPLLs), have also been demonstrated over large bandwidths.[18] Ramos and Seeds have analyzed first and second-order OPLLs, and revealed that first-order OPLLs have better characteristics with higher frequency loop filters.[21] Furthermore, Ramos et al. have proposed an FM synchronizer system using an OPLL combined with optical injection locking to achieve even higher bandwidths.[19]

While these ideas work well in laboratory settings, there tends to be a lack of practicality in the use of coherent detection. Coherent detection is notorious for extreme sensitivity to field and polarization alignment on the photodetector as well as for its added complexity due to the need for a frequency stabilized local oscillator. Lack of robustness, in addition to greater cost, make coherent detection undesirable for many applications. In particular, at MIT Lincoln Laboratory optical links must maintain the highest degree of dependability across a wide range of harsh and demanding military environments. Despite current drawbacks, direct detection is the natural choice. This research hopes to push the limits of direct detection by using optical FM with a direct detection feedback-controlled receiver. This receiver uses a Mach-Zehnder interferometer to convert FM to IM so that direct detection can be used. This FMDD system may provide a means to achieve low optical power direct detection links with SNR and SFDR performance comparable to that of coherent detection links.

Chapter 2

Overview of FM Direct Detection (FMDD) Link

The FMDD link concept is presented in Figure 2-1. The novel aspect of this link is that the demodulator uses a simple direct detection dual-photodetector receiver to demodulate optical frequency modulation. High frequency modulation is obtainable using an electro-optically tunable microchip laser designed by Zayhowski et al.[11] This FM signal is transmitted over single mode (SM) or polarization maintaining (PM) optical fiber and then sent through a demodulator composed of a Mach-Zehnder interferometer, a feedback loop, and dual direct detection photodetectors. The MZI converts frequency modulation to intensity modulation as shown in Figure 2-7, and when the dual-detector receiver is properly biased it cancels out residual AM noise and relative intensity noise (RIN) that would otherwise degrade the signal. The wavelength of the tunable laser is modulated about a center wavelength of $\lambda_o = 1.064 \mu\text{m}$, and the variation in the MZI's output directly correlates to the frequency and amplitude of the input signal. The feedback circuitry determines the input signal by measuring these changes and adjusting the phase difference using an electro-optic phase modulator within the MZI to zero out the modulation and in the process recover it.

2.1 FM Source

The FM source is an electro-optically (EO) tunable diode-pumped solid-state laser (DPSSL) operable at up to 1 GHz deviation frequency. The DPSSL is constructed of a Nd:YAG gain medium and LiTaO₃ EO crystal. A conceptual diagram of this particular device, which was

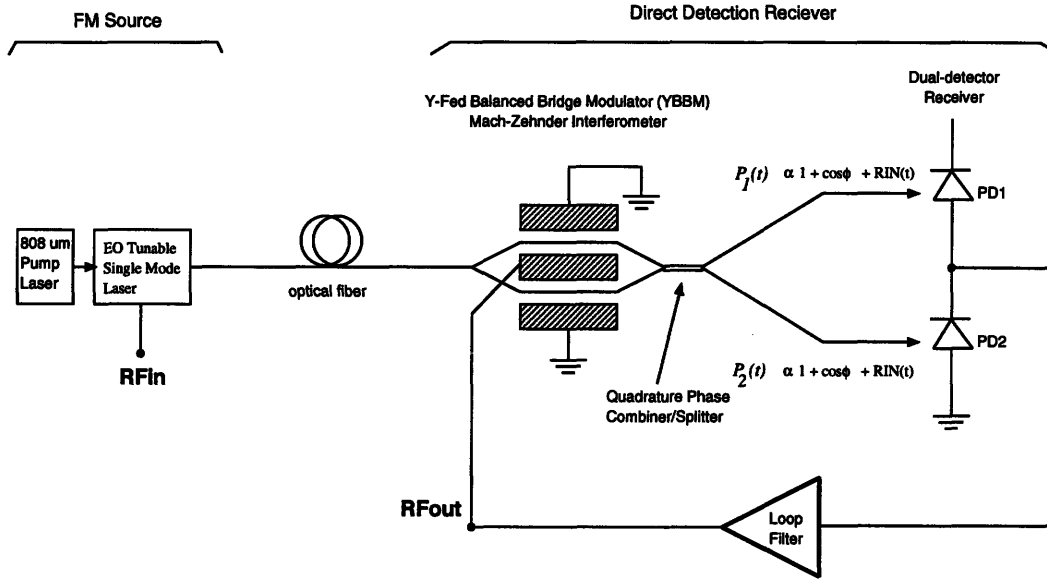


Figure 2-1: Block diagram of FM link using a push-pull YBBM MZI. The output of the two arms of the YBBM give an intensity proportional to $1 \pm \cos(\phi)$, respectively, where ϕ represents the wavelength-dependent and MZI electrode voltage-dependent phase difference between the two arms of the interferometer. The balanced receiver subtracts the two outputs, so that the total photocurrent is proportional to $2\cos(\phi)$.

fabricated in the Quantum Electronics Group at Lincoln Laboratory, is shown in Figure 2-2.[11]¹

A coaxial connection to the laser enables one to apply a modulation voltage that changes the radiation wavelength, as shown in the laser transfer characteristics of Figure 2-3. The voltage applied to the electro-optic crystal changes the refractive index, $n(V)$, of the material through the tensor operation of the linear electro-optic effect, where $n(V) = n_o + \Delta n(V)$ and the electro-optic tensor $\bar{\epsilon}$ acts on a component of the electric field vector:

$$n^2 = \frac{\bar{\epsilon}}{\epsilon_o} \quad (2.1)$$

Variation in n therefore changes the effective optical path length of the material and modulates the fundamental mode around $1.064 \mu\text{m}$. A numerical relation for wavelength and voltage change will be determined in Section 2.1.3.

The Nd:YAG active medium is pumped with a high-power laser diode at a wavelength

¹A more detailed diagram of the laser is contained in the reference.

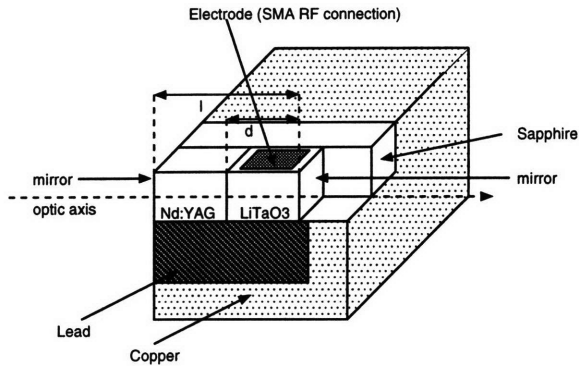


Figure 2-2: Conceptual diagram of electro-optically tunable solid state laser. The pump radiation at 808 nm is incident from the left, and the device lases at 1.064 μm and transmits in the direction of the positive optic axis. The right edge of the LiTaO₃ crystal is mirror coated for transmittance at 1.064 μm and reflectance at 808 nm. Lead and copper are used to dampen low frequency vibrational modes.

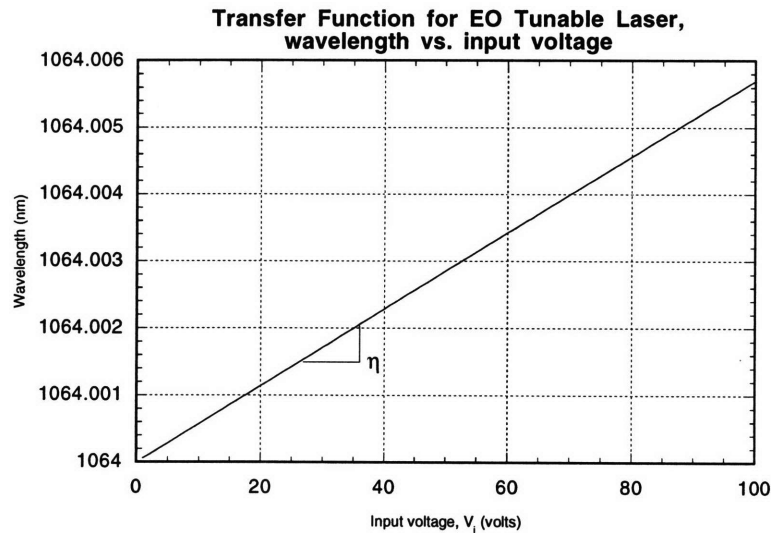


Figure 2-3: Calculated transfer characteristics for electro-optically tunable laser. Wavelength versus voltage tuning sensitivity $\eta \approx 5.7 \times 10^{-14}$ nm/V (or 15 MHz/V) over a 1 GHz bandwidth centered 282 THz (1.064 μm).

of 808 nm, which corresponds to an absorption line of the Nd:YAG. Pumping at this wavelength causes the DPSSL to produce radiation at 1.064 μm , the primary line of YAG. Single mode operation is desirable, so the other modes of YAG are suppressed by the mirror coatings on the edges of the cavity, as illustrated in Figure 2-2. The pump power is kept under one watt, causing the laser to emit about 17 dBm of power at 1.064 μm .

2.1.1 Linewidth and Phase Noise

The FM Nd:YAG DPSSL has a linewidth on the order of 1 MHz, which was measured by a Fabry-Perot cavity as discussed in the next section. As with most solid state lasers, the spectrum is likely narrower than the narrowest width that can be measured by the Fabry-Perot, but this was not verified. Optical phase and frequency noise were not been measured but they are expected to be comparable if not superior to that of a semiconductor laser.

2.1.2 Spectrum Measurements

All FM systems ideally require a single-mode carrier, and our analysis in Chapter 3 relies on the source operating single mode. A Scanning Fabry-Perot Spectrum Analyzer (Newport SuperCavity SR-150) was used to measure the spectrum of the tunable laser. The SuperCavity is an extremely high finesse non-confocal cavity, so testing for single mode behavior is difficult because the input laser beam must be precisely aligned to mode match to the cavity. Additionally, an optical isolator is necessary to prevent feedback to the laser because of the high-finesse mirrors. The SuperCavity is highly accurate for measuring tuning, however, and it can detect if the center wavelength of the YAG laser varies by less than 1 kHz. A linear graph of the power spectrum versus frequency for no electrode bias displayed in Figure 2-4 covers nine free spectral ranges (FSRs) of the cavity. The FSR is 3 GHz, so this tells us the separation of each major peak and in turn a rough estimate for the laser linewidth, which appears roughly 10 kHz. Perfect mode matching over all FSRs is difficult to achieve, so single-mode behavior is hard to observe. Data in Figure 2-4 show the laser to be operating near single-mode where the multiple spikes are due to the SuperCavity's small FSR compared to that of the laser's (90 GHz). Single-mode behavior to within $\pm .1$ nm (26 GHz) is verified using a digital broadband optical spectrum analyzer. A more thorough method for accurately measuring the extent of multimode behavior of the laser would be to use self-heterodyning with coherent detection.

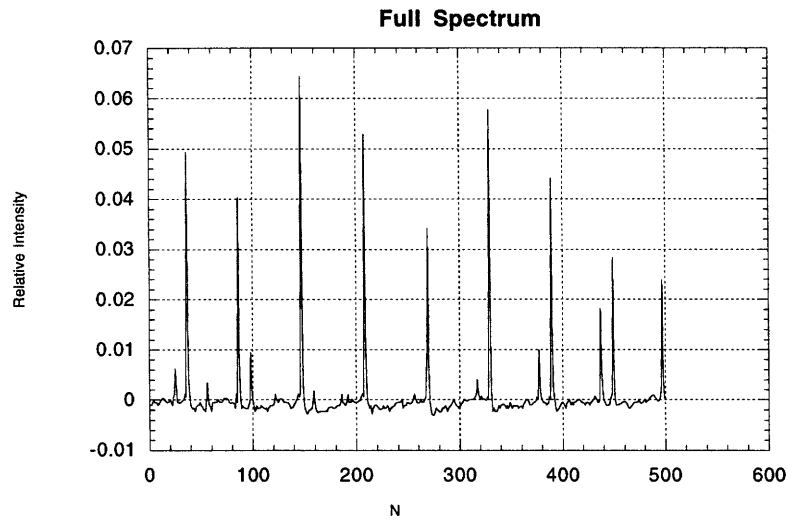


Figure 2-4: Measurement of tunable Nd:YAG laser spectrum using SuperCavity scanning Fabry-Perot. Horizontal axis N represents optical frequency normalized to free-spectral range (FSR) of cavity and referenced to center wavelength ($\nu_o = 282.000$ THz): $N \triangleq \frac{400}{\text{FSR}}(\nu - \nu_o)$. FSR of cavity is 3 GHz, with plot spanning 1.25 FSRs. Laser's FSR is about 90 GHz, so numerous spikes are either due to convolved (*i.e.*, nonadjacent) multimode behavior, or more likely, improper mode-matching to the SuperCavity. We measure each peak to have FWHM ~ 1 MHz.

2.1.3 Tuning Sensitivity and Wavelength Displacement

The microchip laser used has a tuning sensitivity of 15 MHz/V over a bandwidth of about 1 GHz as measured by Zayhowski et al.[11]. This was verified at DC using the SuperCavity setup to show that a tuning voltage of 200 VDC moves the spectrum by $15 \text{ MHz} \times 200 = 3\text{GHz}$, corresponding to one full FSR of the cavity.

Figure 2-3 indicates knowledge of the wavelength tuning, $\Delta\lambda$, as linearly related to the input voltage, V_{in} , by the proportionality constant η . This link parameter η in m/V is necessary for modeling the link characteristics, so it is calculated from the experimental frequency tuning quantity of 15 MHz/V provided in [11] and verified above at DC.

The dispersion relation provides the change in wavelength with respect to frequency at λ_o .

$$\frac{\Delta\lambda}{\Delta\nu} = -\frac{c}{\nu^2} = -\frac{\lambda^2}{c} \quad (2.2)$$

A simple units conversion gives

$$\eta = \frac{\Delta\nu}{\Delta V} \cdot \frac{\Delta\lambda}{\Delta\nu} \quad (2.3)$$

The quantity 15 MHz/V is substituted into (2.2) to arrive at

$$\eta = 5.7 \cdot 10^{-14} \text{m/V} \quad (2.4)$$

To verify the result in (2.4) the derivation of η starts with the linearity assumption in (2.5).

$$\lambda(V_{in}) = \lambda_o + \eta V_{in} \quad (2.5)$$

The laser's center wavelength λ_o in (2.5) is $1.0641 \mu\text{m}$. The geometry depicted in Figure 2-2 is treated as a mirror end-faced Fabry-Perot cavity with multiple resonant frequencies, yielding (2.6).

$$\lambda(V_{in}) = \frac{2n(V_{in})l}{m} \quad (2.6)$$

The longitudinal mode number of the cavity is represented as m and the cavity optical index $n(V_{in})$ is a function of V_{in} through the electro-optic effect. The electro-optic effect is

linear so $n(V_{in})$ can be separated into

$$n(V_{in}) = \bar{n} + \Delta n(V_{in}). \quad (2.7)$$

The quantity \bar{n} is the average index of the (Nd:YAG + LiTaO₃) composite cavity, weighted by the lengths of the individual sections. Along the optic axis the Nd:YAG and LiTaO₃ sections have lengths 0.5 mm and 1.0 mm, respectively, yielding a total length $l = 1.5$ mm. The optical indexes of Nd:YAG and LiTaO₃ are $n_Y = 1.5$ and $n_L = 2.2$, respectively.

$$\bar{n} = \frac{n_Y + 2n_L}{3} \quad (2.8)$$

$$\bar{n} \cong 2.0 \quad (2.9)$$

The linear electro-optic effect produces a change in the optical index of the cavity that is proportional to an applied electric field. The rate of change Δn must be scaled by the fraction of the cavity occupied by the electro-optic LiTaO₃ crystal. The largest electro-optic coefficient for LiTaO₃ is $r_{33} = 3.6 \cdot 10^{-11}$ m/V [22], and the electrode spacing across the laser's electro-optic material is $d = 1.0$ mm.

$$\Delta n(V_{in}) = 2/3 \frac{n_L^3 r_{33} \Gamma}{2d} V_{in} \quad [23] \quad (2.10)$$

The overlap integral between the field and the optical mode is denoted as Γ , where $0 < \Gamma < 1$. Using (2.10), the expression (2.7) is substituted into (2.6) yielding

$$\lambda(V_{in}) = \frac{2\bar{n}l}{m} + \frac{2ln_L^3 r_{33} \Gamma}{3md} V_{in}. \quad (2.11)$$

This expression is combined with (2.5) to give

$$\lambda_o = \frac{2\bar{n}l}{m}, \quad (2.12)$$

$$\eta = \frac{2ln_L^3 r_{33} \Gamma}{3md}. \quad (2.13)$$

The mode number $m = 5,545$ is solved from (2.12). Without evaluating the integral Γ , we can only determine an upper bound for η . For full overlap of the fields $\Gamma = 1$, hence

$$\eta \leq \frac{2ln_L^3 r_{33}}{3md} \quad (2.14)$$

$$\eta \leq 7.0 \cdot 10^{-14} \text{m/V}. \quad (2.15)$$

The experimental result for η in (2.4) is plausible since it falls within the bound set by (2.15).

2.2 Demodulator

The demodulator design is a simple yet novel application of FM discrimination to optical detection. The frequency modulated optical signal passes through a Mach-Zehnder Interferometer with a variable voltage-controlled path length difference. A feedback loop nulls the error signal caused by deviation in the output amplitude of the interferometer. The system is designed around a center wavelength of 1.064 μm .

To make the demodulation scheme insensitive of relative intensity noise (RIN) from the laser source and to magnify the received signal power, a Y-fed Balanced Bridge Modulator (YBBM) would ideally be used, as shown in Figure 2-1. The phase difference between the two arms of the MZI is generalized as ϕ and the existence of additive RIN is denoted by $RIN(t)$. The non-DC outputs of the YBBM are inverted with respect to each other, so that

$$P_1(t) \propto 1 + \cos(\phi) + RIN(t), \quad (2.16)$$

and

$$P_2(t) \propto 1 - \cos(\phi) + RIN(t), \quad (2.17)$$

where the proportionality constants for (2.16) and (2.17) are equal. By using a balanced receiver shown in Figure 2-1 similar to that found in the heterodyne receiver of [24], the total output is the difference of $P_2(t)$ and $P_1(t)$. The difference current seen by the feedback electronics is just

$$i_f \propto -2\mathcal{R} \cos(\phi), \quad (2.18)$$

and therefore the RIN and even amplitude of the optical signal may be neglected.

Unfortunately a YBBM MZI was not readily available for use at 1.064 μm , so we instead

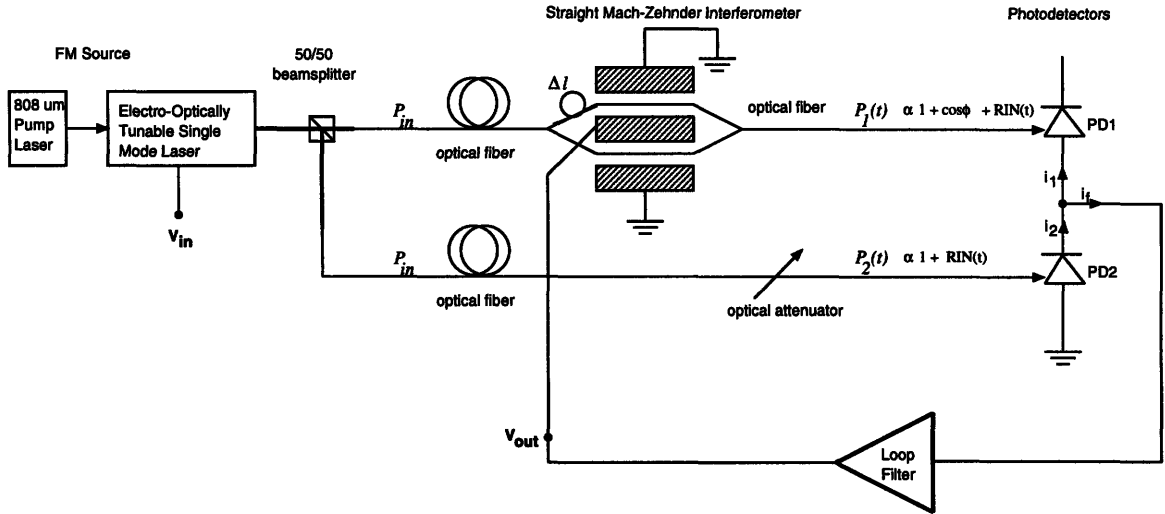


Figure 2-5: Block diagram of FM link using standard MZI. The optical attenuation is set to -3 dB, scaled by the fiber-to-fiber MZI insertion loss, t_{ff} .

use the design shown in Figure 2-5, which uses a conventional single-output MZI. To achieve cancellation of DC and RIN terms the original beam is sent through a 50/50 beamsplitter and the non-demodulated leg is attenuated by an amount equal to the MZI insertion loss $10 \log_{10}(t_{ff})$ plus -3 dB for the bias point. The half-power (-3 dB) operating point will be explained in Section 2.2.1. Note that the non-YBBM link design, in contrast to the YBBM link shown in Figure 2-1, requires knowing an additional free-parameter, t_{ff} .

The equations in Section 2.2.2 will demonstrate how the feedback circuit becomes sensitive only to variations in amplitude caused by wavelength changes.

2.2.1 Mach-Zehnder Interferometer (MZI)

The most common type of external modulator is based on a Mach-Zehnder interferometer (MZI), which is an interferometer with two beamsplitters.[23] An MZI modulator is created by varying the length of the two arms with respect to each other. Most MZIs achieve modulation of the path lengths using electro-optic (EO) material.[2, 23] When an electric field is applied across the EO material, the refractive index and optical phase velocities change accordingly in each arm of the interferometer. The optical signal slows down or speeds up, depending on the direction of change of the optical index. When the fields recombine at the output of the modulator, the extent to which they combine constructively

depends on the phase change applied between the arms. A push-pull layout is often used that applies equal but opposite electric fields (hence phases) to each branch so that the total applied phase imbalance is doubled.

The optical output intensity of a non-push-pull MZI, as used in this FMDD link, is described generally by (2.19).

$$P_{out} = \frac{P_{in}}{2}(1 + \cos \phi) \quad (2.19)$$

The phase ϕ is a complicated expression that is separated into

$$\phi = \psi_1 + \psi_2. \quad (2.20)$$

The voltage applied to the EO modulator electrode (in this case V_{out}) varies the phase ϕ linearly due to the electro-optic effect, so (2.19) indicates that the intensity P_{out} varies sinusoidally with V_{out} . The parameter V_π sets the sinusoidal periodicity through the physical characteristics of the modulator, and V_π defines the voltage that induces a π phase shift to ϕ . Since the MZI is an interferometer, the amount of intensity fluctuation due to electro-optic modulation of the optical path length depends on the wavelength. As the wavelength defined in (2.5) $\lambda(V_{in})$ increases, the change in intensity due to a fixed amount of path length variation decreases. This discussion intuitively leads to an expression for the first phase terms, ψ_1 :

$$\psi_1 = \frac{\pi V_{out} \lambda_o}{V_\pi \lambda(V_{in})} \quad (2.21)$$

The other phase variation of ϕ is due purely to interferometric behavior of the MZI. If an interferometer has exactly zero path difference in the two arms, then the output intensity is independent of wavelength and we call this a white-light interferometer. When a path length difference, $\Delta\ell$, is introduced, the change in output intensity for a given wavelength change will increase as $\Delta\ell$ increases. This explains the second phase term ψ_2 , which becomes

$$\psi_2 = \frac{2\pi \Delta\ell}{\lambda(V_{in})}. \quad (2.22)$$

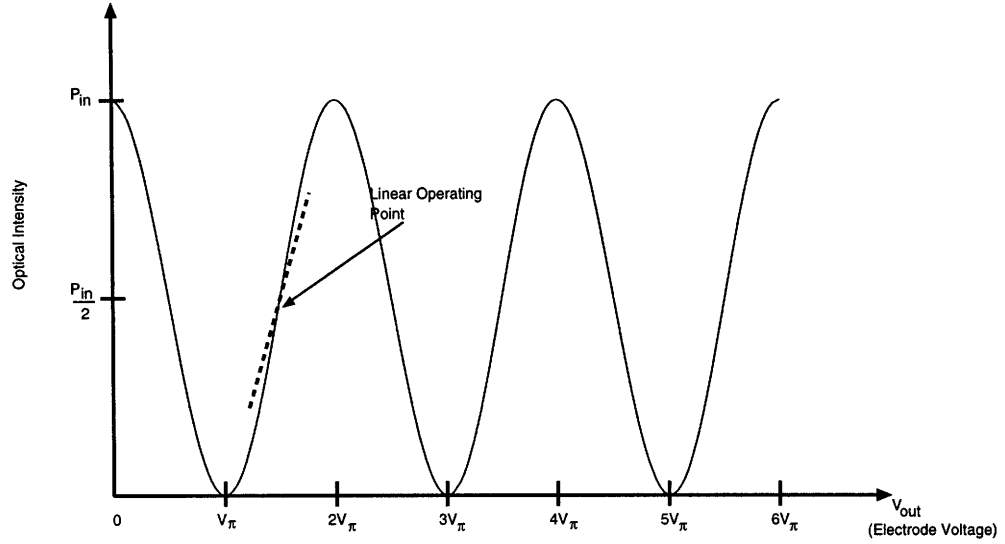


Figure 2-6: Mach-Zehnder Interferometer intensity versus electrode voltage (defined in our link as V_{out}) transfer function shown in (2.18). It is assumed that $\Delta\ell = 0$ so that the transfer function has no phase offset under zero voltage. Also $\lambda \rightarrow \lambda_o$. V_π is shown as the switching voltage or voltage that swings the phase by π . The linear (-3 dB) operating point is shown also. Arbitrary units are shown on both axes.

The explicit transfer function for the non-push-pull MZI can now be written as

$$P_{out} = \frac{P_{in}}{2} \left[1 + \cos \left(\frac{\pi V_{out} \lambda_o}{V_\pi \lambda(V_{in})} + \frac{2\pi \Delta\ell}{\lambda(V_{in})} \right) \right]. \quad (2.23)$$

As discussed above the wavelength λ can be expressed as a function of the input modulation voltage, V_{in} , from (2.5). The transfer function (2.23) shows a highly nonlinear relation between the output voltage on the MZI and the input voltage on the laser. The transfer function (2.23) is plotted versus electrode voltage V_{out} in Figure 2-6 for no wavelength modulation ($\lambda = \lambda_o$) and zero path length difference ($\Delta\ell = 0$).

In order to get the most efficiency from the wavelength modulation of the laser, the interferometer must possess a large path length difference, as is evident from (2.23). One way to detect small wavelength variations in λ would be to have a small V_π , however this is fixed to between 5 and 10 Volts by the design of the electro-optics components, and V_{out} is also limited to within reasonable ranges by the available feedback electronics. When $\Delta\ell$ is larger than a wavelength, the response due to a given wavelength deviation improves substantially with $\Delta\ell$.

The arm-imbalance $\Delta\ell$ has an inverse relation with the bandwidth ($\Delta\nu$) between adjacent peaks and nulls of the intensity-optical frequency MZI transfer function, shown in Figure 2-7. The sinusoidal transfer function (2.23) is rewritten in terms of optical frequency, ν , by using the fact that

$$\frac{1}{\lambda} = \frac{\nu n}{c}. \quad (2.24)$$

The transfer function (2.23) then becomes

$$P_{out} = \frac{P_{in}}{2} \left[1 + \cos \left(\frac{\pi V_{out} \lambda_o}{V_{\pi} \lambda (V_{in})} + \pi \frac{\nu}{\Delta\nu} \right) \right], \quad (2.25)$$

where

$$\Delta\nu = \frac{c}{2n\Delta\ell} \quad [25]. \quad (2.26)$$

The physical meaning of $\Delta\nu$ is clear from Figure 2-7.

It is important to note that when $\Delta\ell$ approaches zero $\Delta\nu$ correspondingly goes to infinity. Under this condition the MZI functions as a white light interferometer. This is desirable for applications using broadband optical signals, such as WDM communication systems or IM links. In Figure 2-8 the interferometric behavior of an integrated half-coupler MZI is measured.² A half-coupler modulator uses a double pass interferometer that gives a periodic transfer with major and minor peaks. The bandwidth between major peaks and nulls $\Delta\nu$ can be computed from (2.2), giving $\Delta\nu \approx 5 \cdot 10^{12}$ Hz. This bandwidth corresponds to $\Delta\ell \approx 20 \mu\text{m}$ using (2.26), hence, $\Delta\ell$ must increase substantially to detect frequency modulation on the electro-optically tuned laser used in this experiment. The modulation bandwidth resulting from the laser tuning range is under 100 MHz so (2.26) indicates that the MZI should have about one meter of path length difference.

Most integrated MZIs are built symmetrically, and even those that have been specifically constructed with an arm-imbalance only possess small (≤ 1 cm) $\Delta\ell$ quantities.[25] For this experiment, the best method for creating a large $\Delta\ell$ is to construct the MZI out of polarization-maintaining (PM) optical fiber, 3 dB PM couplers, and a phase modulator. The non-push-pull fiber MZI is shown in Figure 2-9. A fusion splicer is used to change fiber lengths, resulting in a changed $\Delta\ell$.

²Measurement courtesy of R.G. Helkey.

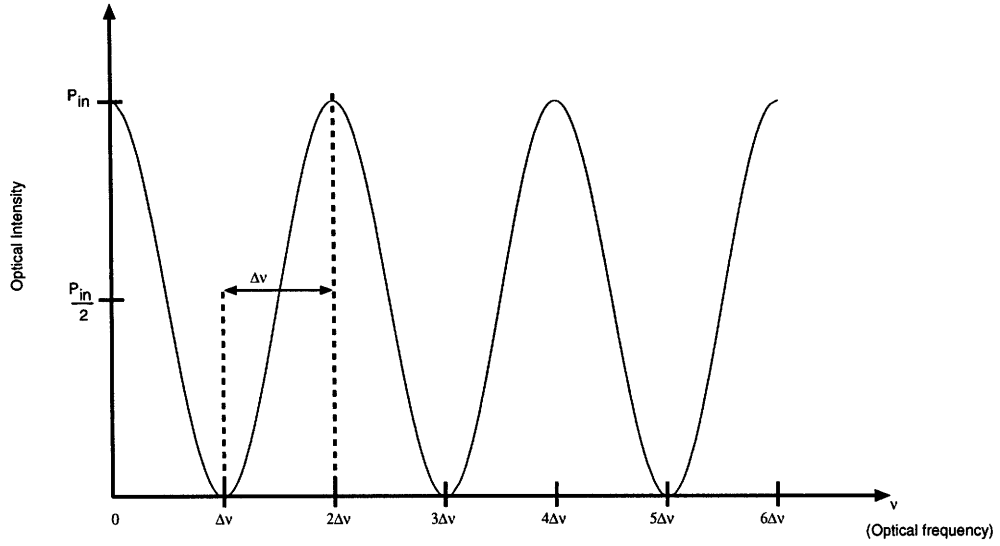


Figure 2-7: Mach-Zehnder Interferometer intensity versus optical frequency transfer function, assuming zero phase difference at zero $\Delta\nu$. The peak-to-null spacing $\Delta\nu$ is related to $\Delta\ell$ by (2.11). Arbitrary units are shown on both axes.

2.2.2 Dual Photodetector Balanced Receiver

As Figure 2-5 shows, a beamsplitter is used at the input of the modulator so that half of the light is coupled through an optical attenuator and the other half goes through the modulator. Each of these laser beams is applied to the two series photodetectors, and the equations below show that the difference current into the feedback circuitry should stabilize to zero when the power is evenly balanced. As discussed above, the primary reason for this is to cancel as much as possible of the RIN and amplitude noise created by the EO tunable Nd:YAG laser.

From the diagram in Figure 2-5, the feedback current i_f results from

$$i_f = i_2 - i_1. \quad (2.27)$$

Next express i_f in terms of the optical powers from the MZI and reference arms by using the responsivity of the detectors, \mathcal{R} .

$$i_f = \mathcal{R}P_2(t) - \mathcal{R}P_1(t) \quad (2.28)$$

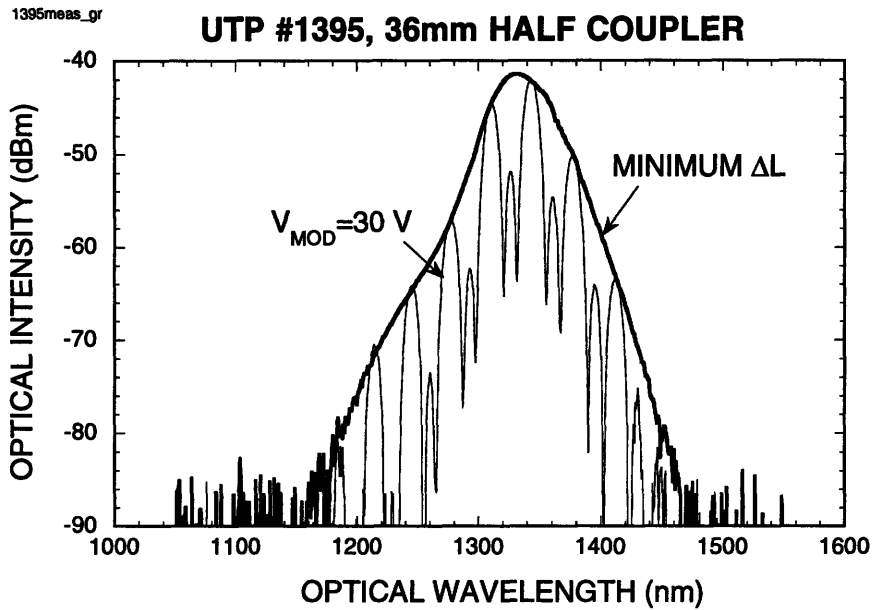


Figure 2-8: Measurement of maximum $\Delta\ell$ in modulator given a broadband optical noise source. For this half-coupler modulator the transfer characteristic is a sum of sinusoids, so alternating hump behavior results. Global maxima exist when the phase difference across the two arms $\phi = m\pi$ and local maxima exist when $\phi = \frac{2m+1}{2}\pi$, ($m = 1, 2, \dots$). The Gaussian-like envelope is due to the spectral characteristics of the source.

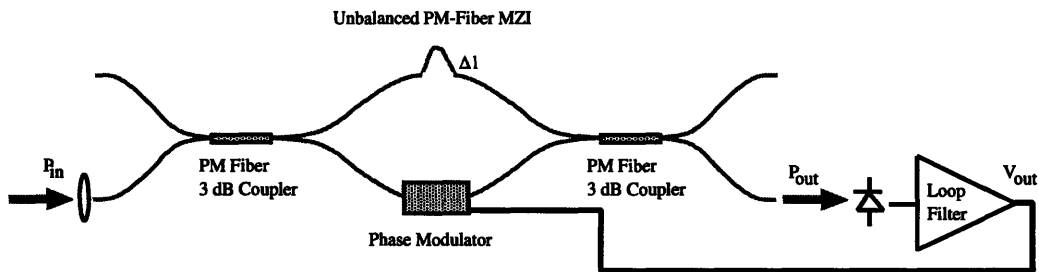


Figure 2-9: Mach-Zehnder Interferometer constructed out of PM optical fiber, 3 dB couplers, and EO phase modulator. Fixed changes in $\Delta\ell$ are accomplished with a PM fusion splicer.

The initial power at each output of the 50/50 beamsplitter is represented by P_o . The optical attenuation in the reference arm is adjusted so $P_2(t)$ is exactly half of the maximum power available at $P_1(t)$. When this balanced condition holds,

$$i_f = \frac{1}{2}t_{ff}\mathcal{R}P_o - \frac{1}{2}t_{ff}\mathcal{R}P_o \left(1 + \cos\left(\frac{\pi V_{out}\lambda_o}{V_\pi\lambda(V_{in})} + \frac{2\pi\Delta\ell}{\lambda(V_{in})}\right)\right) \quad (2.29)$$

$$i_f = -\frac{1}{2}t_{ff}\mathcal{R}P_o \left(\cos\left(\frac{\pi V_{out}\lambda_o}{V_\pi\lambda(V_{in})} + \frac{2\pi\Delta\ell}{\lambda(V_{in})}\right)\right). \quad (2.30)$$

and the DC terms of i_f are canceled out.

The feedback loop is designed to null i_f so the argument of the cosine term in (2.30) is maintained at some odd integer multiple of $\frac{\pi}{2}$. Setting this cosine argument in this way yields (2.31), which is the transfer function of the forward path of the feedback loop.

$$V_{out}\frac{\pi\lambda_o}{V_\pi} = \lambda(V_{in}) \left[\frac{2m+1}{2}\pi - \frac{2\pi\Delta\ell}{\lambda}\right], \quad m = 0, 1, 2, \dots \quad (2.31)$$

When running closed loop, the feedback loop is not constrained by (2.31). Instead the small signal output moves about the bias point, represented by the linear relation in (2.31). To determine the full transfer function of the system, a feedback loop analysis will be performed in Section 3.

This equation does not really yield the transfer function of the system. (Recall that (2.5) gives a linear relation between input voltage and wavelength.) In actuality, since the bias point will be moving slightly around a linear part of the curve where (2.31) holds, it is necessary to do a feedback loop analysis to determine what kind of integrator and gain stages are needed.

2.2.3 Feedback Loop

The demodulator feedback circuit is represented in block diagram form in Figure 2-10. This approach uses a non-inverting buffer amplifier to convert the current i_f into a voltage; the voltage then passes through a first-order integrator stage. Amplification is added to increase the loop gain, and a current amplifier is used as a buffer to drive a 50 Ω termination on the MZI phase modulator.

The entire loop is designed to be flat over the working range and then fall off as $1/s$ from the integrator characteristics. The link is demonstrated at 4 MHz so the -3 dB frequency

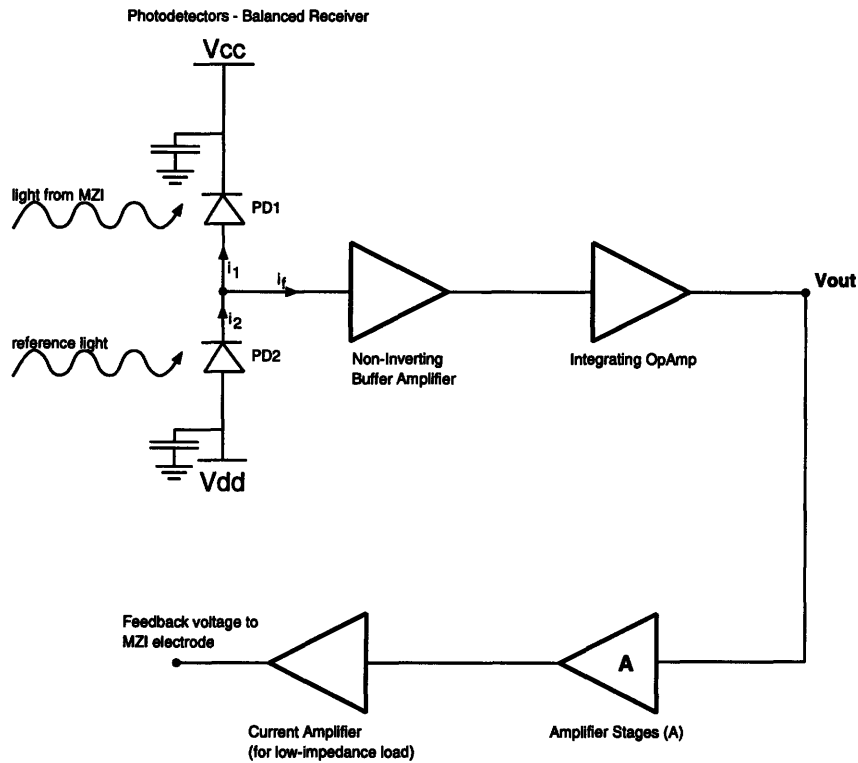


Figure 2-10: Major circuit components of first-order integrating FM demodulator. Most of the amplifiers shown are standard Op Amps. The dual photodetector receiver is shown with bias capacitors to allow RF paths to ground while applying reverse bias voltages to the photodetectors; the photodetector midpoint is maintained at a virtual ground due to the negative input characteristics of the Op Amp. The non-inverting buffer amplifier converts current i_f to voltage.

Chapter 3

Link Modeling

This chapter presents the analysis for determining the transfer characteristic of the link. The loop filter circuit design and the MZI transfer characteristics are carefully analyzed to study gain, noise figure and dynamic range. The model results will be compared to experimental values in Chapter 4.

3.1 Loop Gain

The loop gain analysis characterizes the intensity of the optical signal as it passes through the MZI. A small-signal is used that defines input and output voltage as a sum of large-signal DC and small-signal AC terms.

$$\mathbf{V}_i = V_i + v_i \quad (3.1)$$

$$\mathbf{V}_o = V_o + v_o \quad (3.2)$$

An affine relationship, *i.e.*, linear with no offset, is needed between incremental input voltage, v_i , and incremental output voltage, v_o . To linearize the system, the link is analyzed in a linear gain-block manner, as shown in Figure 3-1. This block diagram shows the linearized components of the FMDD link. The laser is modeled as the input transfer function \mathbf{H}_1 , which relates v_i to the \tilde{p}_1 component of the incremental intensity p_{out} as shown on Figure 3-1. Similarly, \mathbf{H}_3 models the transfer function from v_o to the other incremental intensity component \tilde{p}_2 . The forward path of the link, including the photodetector receiver,

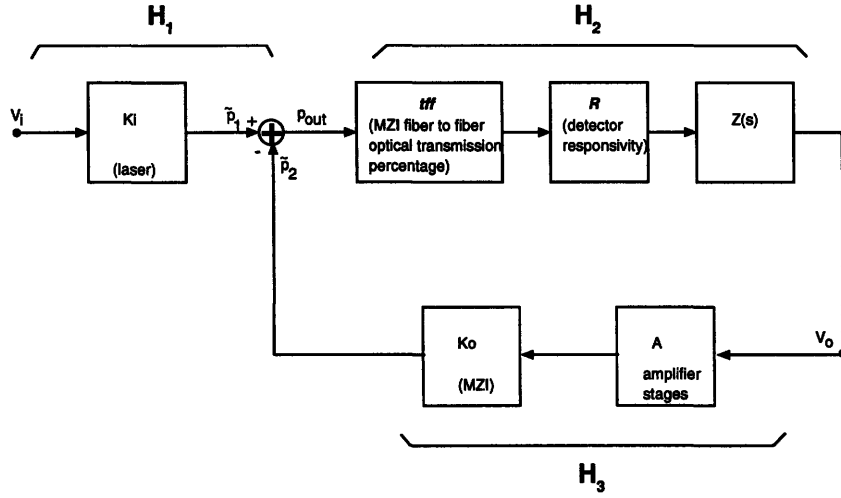


Figure 3-1: Explicit FM demodulator gain block diagram showing small signal model relationships for Intensity Model.

fiber loss, and loop filter, is characterized by H_2 .

The output intensity of the MZI, P_{out} , can be separated into incremental and DC components, as in (3.3).

$$P_{out} = P_{DC} + p_{out}(t) \quad (3.3)$$

The DC component is represented by P_{DC} and the incremental is represented by $p_{out}(t)$. (Refer back to (2.23).) The balanced receiver, represented by the adder \oplus in Figure 3-1, is designed to subtract the DC component P_{DC} from (3.3) leaving us with just $p_{out}(t)$ at the loop filter input. In reality the balanced receiver performs subtraction *after* the photodetectors convert the optical signal to an RF signal, but the components are linear, time-invariant so the forward path can be rearranged without altering the overall loop behavior. This intuitively allows t_{ff} and \mathcal{R} to be placed just prior to the loop filter $Z(s)$ as depicted in Figure 3-1.

3.1.1 Linearization Method

The gain-block model indicates that the quantity p_{out} must be a separable function of v_i and v_o . Unfortunately, p_{out} is highly nonlinear between the input and output since

$$p_{out} = \frac{P_{in}}{2} \cos \left(\frac{\pi \mathbf{V}_o \lambda_o}{V_\pi (\lambda_o + \eta \mathbf{V}_i)} + \frac{2\pi \Delta \ell}{\lambda_o + \eta \mathbf{V}_i} \right). \quad (3.4)$$

A first order Taylor expansion in two dimensions is performed on (3.4) in the following manner, where the square brackets $[...]_{AC}$ indicate to take the AC terms only:

$$p_{out}(\mathbf{V}_i, \mathbf{V}_o) \cong \left[v_i \frac{\partial}{\partial \mathbf{V}_i} (p_{out}) \Big|_{\mathbf{V}_i=0, \mathbf{V}_o=V_\pi/2} \right]_{AC} + \left[v_o \frac{\partial}{\partial \mathbf{V}_o} (p_{out}) \Big|_{\mathbf{V}_o=\frac{V_\pi}{2}, \mathbf{V}_i=0} \right]_{AC} \quad (3.5)$$

$$p_{out}(\mathbf{V}_i, \mathbf{V}_o) \triangleq K_i v_i + K_o v_o \quad (3.6)$$

The calculation in (3.5) yields

$$\frac{\partial}{\partial \mathbf{V}_i} (p_{out}) \Big|_{v_i=0} = P_{in} \eta \left(\frac{\pi \mathbf{V}_o \lambda_o + 2\pi \Delta \ell V_\pi}{2V_\pi \lambda_o^2} \right) \sin \left(\frac{\pi \mathbf{V}_o \lambda_o + 2\pi \Delta \ell V_\pi}{V_\pi \lambda_o} \right) \quad (3.7)$$

$$K_i \cong P_{in} \eta \left(\frac{\pi \Delta \ell}{\lambda_o^2} \right) \cos \left(\frac{2\pi \Delta \ell}{\lambda_o} \right), \quad (3.8)$$

for $\Delta \ell \gg \lambda_o$. The model relies on the assumption that the MZI transfer characteristic (2.23) is maintained at the half power point so that the phase obeys (2.31). In reality the loop filter automatically adjusts \mathbf{V}_o to preserve (2.31). Fixing \mathbf{V}_o in this model therefore limits us to choosing values of $\Delta \ell$ that are multiples of λ_o , even though this does not matter in practice. K_i may be reduced to

$$K_i = P_{in} \eta \left(\frac{\pi \Delta \ell}{\lambda_o^2} \right). \quad (3.9)$$

By similar reasoning,

$$K_o = -P_{in} \frac{\pi}{2V_\pi} \cos \left(\frac{2\pi \Delta \ell}{\lambda_o} \right). \quad (3.10)$$

$$K_o = -P_{in} \frac{\pi}{2V_\pi}. \quad (3.11)$$

3.1.2 Gain Coefficients

The equations in Section 3.1.1 indicate that the input path \mathbf{H}_1 becomes

$$\mathbf{H}_1 \triangleq \frac{\tilde{p}_1}{v_i} = K_i. \quad (3.12)$$

The forward path includes the photodetector responsivity, \mathcal{R} , and the fiber-to-fiber optical insertion loss of the MZI, t_{ff} .¹ The transimpedance loop filter $\mathcal{Z}(s)$ represents the first order integrator. From Figure 3-1

$$\mathbf{H}_2 \triangleq \frac{V_o}{p_{out}} = t_{ff} \mathcal{R} \mathcal{Z}(s). \quad (3.13)$$

The feedback path H_3 includes additional gain A as well as the MZI modeled as K_o . It is concluded that

$$\mathbf{H}_3 \triangleq \frac{\tilde{p}_2}{v_o} = AK_o. \quad (3.14)$$

3.1.3 Gain and Bandwidth Calculation

The definition of small-signal voltage gain is

$$g_v \triangleq \frac{v_o}{v_i}. \quad (3.15)$$

It follows from the gain block diagram in Figure 3-1 that g_v becomes

$$g_v = \frac{\mathbf{H}_1 \mathbf{H}_2}{1 + \mathbf{H}_2 \mathbf{H}_3}. \quad (3.16)$$

The expressions (3.12), (3.13), (3.14) can be inserted into (3.16) to give

$$g_v = \frac{t_{ff} \mathcal{R} P_{in} \Delta \ell \eta \frac{\pi}{\lambda_o^2} \mathcal{Z}(s)}{1 - \frac{t_{ff} A \mathcal{R} P_{in} \mathcal{Z}(s) \pi}{2V_\pi}} \quad (3.17)$$

The transimpedance amplifier is an integrating op-amp with a feedback resistor (R_2),

¹To express magnitude loss t_{ff} in terms of dB loss, $t_{ff} = 10^{-\frac{dB}{10}}$.

matched to an input resistor R_1 placed in a non-inverting op-amp. Hence $\mathcal{Z}(s)$ is

$$\mathcal{Z}(s) = \frac{R_1}{R_2 C s}, \quad s = j\omega. \quad (3.18)$$

The small signal power gain, g_p , under the condition of perfect impedance matching between the input and output is the square of (3.17). The gain, G in dB form is shown below in (3.21).

$$g_p = \left| \frac{v_o}{v_i} \right|^2 \quad (3.19)$$

$$G \triangleq 10 \log_{10}(g_p) \quad (3.20)$$

$$G = 20 \log_{10} \left(\left| \frac{t_{ff} \mathcal{R} P_{in} \Delta \ell \eta \frac{\pi}{\lambda_2} \mathcal{Z}(s)}{1 - \frac{t_{ff} A \mathcal{R} P_{in} \mathcal{Z}(s) \pi}{2V\pi}} \right| \right) \quad (3.21)$$

The power gain (in dB) is plotted logarithmically versus both $\Delta \ell$ (referenced to 1 m) and RF frequency (referenced to 1 rad/sec) in Figure 3-2. The gain grows with $\Delta \ell$ because the bandwidth between successive peaks of the interferometer transfer function narrows, however the gain rolls off with frequency beyond a breakpoint due to the bandwidth limitation of the feedback electronics. Behavior of gain versus $\Delta \ell$ is more evident in Figure 3-3, which is a slice of Figure 3-2 at a fixed frequency of 1 MHz with G plotted logarithmically versus $\Delta \ell$. The bandwidth of the loop is evident from a slice of Figure 3-2 shown in Figure 3-4. This figure plots G logarithmically versus ω at a fixed arm imbalance of $\Delta \ell = 1.080$ m.

3.2 Alternative Gain Formulation (Phase Model)

The gain analysis may also be done by considering the phase differences within the MZI. Figure 3-5 depicts the gain block diagram used in this method of modeling the feedback control loop. Since the transfer function presented in (2.23) is composed of two phase terms, each can be studied independently. The second term (denoted below as φ_1) is a measure of the phase variation due to FM on the laser. This effect is external to the feedback loop. The first phase term (denoted φ_2) is controlled directly by the feedback loop. Although it

Gain Bode Plot (dB) versus $2\pi \cdot f$ (rad/sec) and Delta (m)

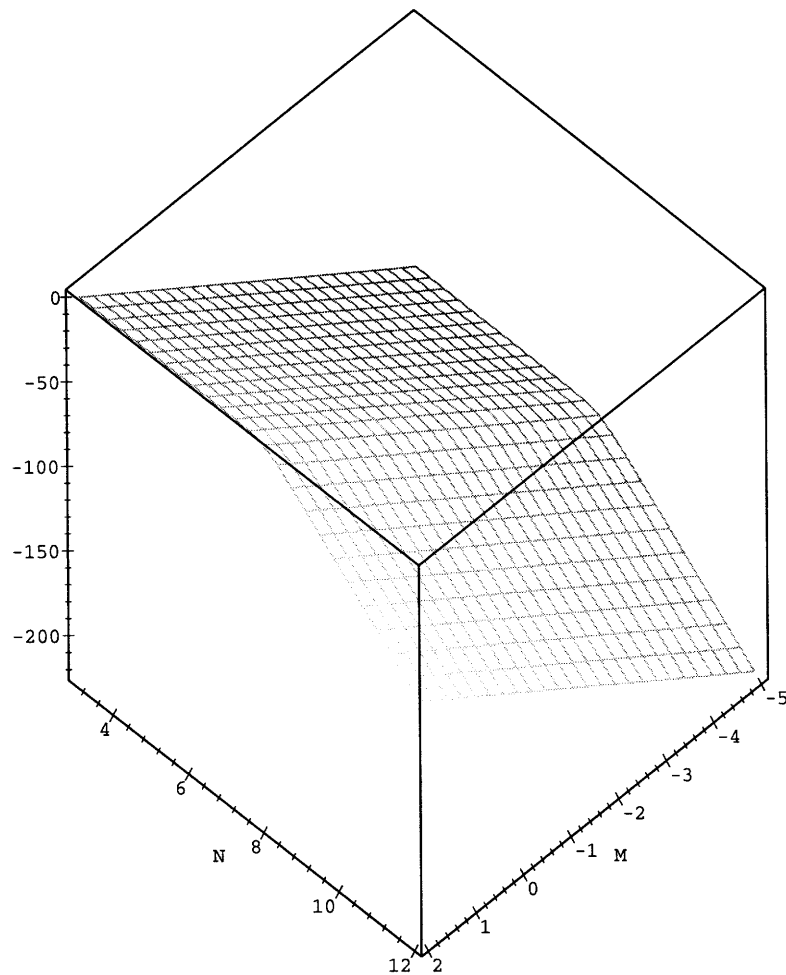


Figure 3-2: Three dimensional bode plot of power gain (dB) versus $\log_{10}(\frac{\Delta \ell}{1\text{m}})$ for FM link. Path length difference axis is labelled by $M \triangleq \log_{10}(\frac{\Delta \ell}{1\text{m}})$. Frequency axis is labeled by $N \triangleq \log_{10}(\frac{\omega}{1\text{rad/sec}})$. Below breakpoint frequency, gain is a flat -46 dB with ~ 1 m of path length difference; after breakpoint frequency response falls of at -20 dB/dec. Plot shown for V_o of 2.5 V, V_π of 5.0 V, and \mathcal{R} of .4 A/W. P_{in} is 4 mW and t_{ff} set to 0.25. See Table 3-1 for other parameters.

Link Gain (dB) versus $\log_{10}(\Delta\ell)$, Intensity Model

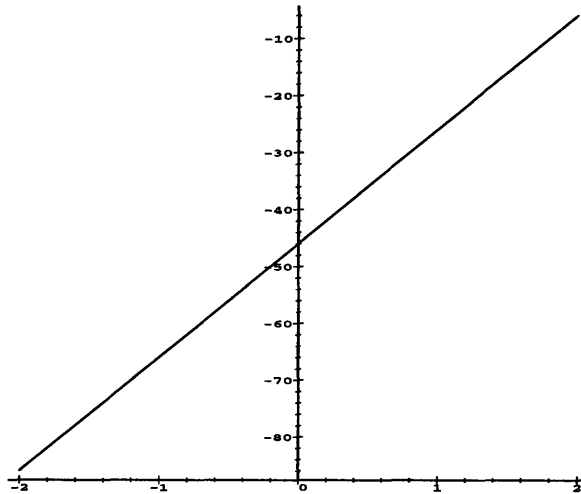


Figure 3-3: Intensity Model Gain in dB plotted versus $\log_{10}(\frac{\Delta\ell}{1m})$ at a fixed frequency 1 MHz. This plot is a two-dimensional slice of Figure 3-2.

Modelled Link Gain (dB) versus $\log_{10}(\omega)$

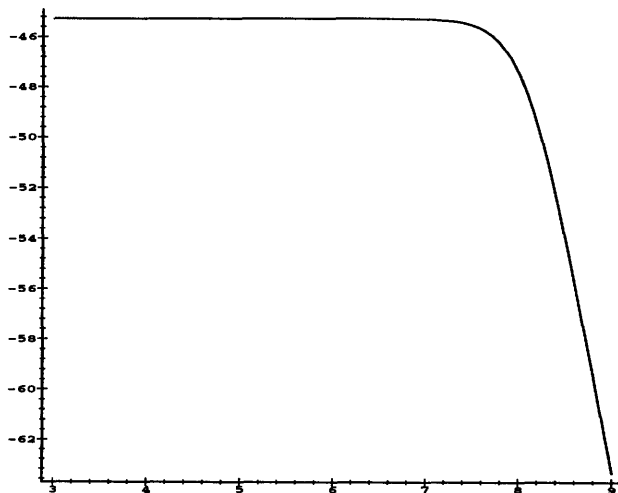


Figure 3-4: Intensity Model Gain in dB versus $\log_{10}(\frac{\omega}{1rad/sec})$ at a fixed path length difference $\Delta\ell = 1.080$ m. The model shows a -3 dB breakpoint of 20 MHz. This plot is a two-dimensional slice of Figure 3-2.

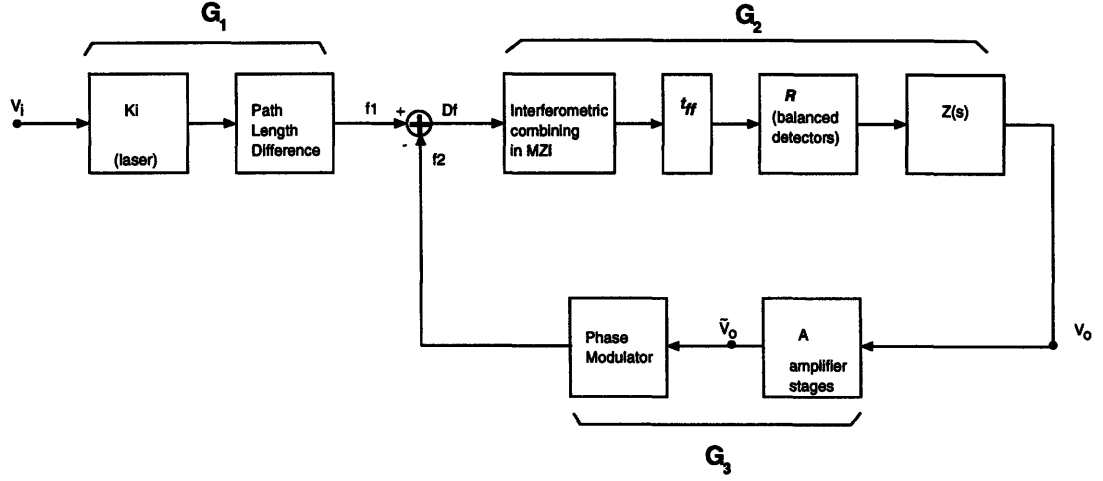


Figure 3-5: Small-signal FM link demodulator gain block diagram using Phase Model.

is not first-order, it has a very weak dependence on input voltage, hence

$$\varphi_2 = \frac{\pi \tilde{V}_{out} \lambda_o}{v_\pi \lambda(V_{in})} \cong \frac{\pi \tilde{V}_{out}}{v_\pi}. \quad (3.22)$$

This simplification allows the feedback loop to be modeled using a linear first-order system.

3.2.1 Input

The input stage is nonlinear in λ since

$$\varphi_1(V_{in}) = \frac{2\pi \Delta \ell}{\lambda(V_{in})}. \quad (3.23)$$

A first-order Taylor series about λ_o can be used to expand (3.23). Substituting (2.5) into the Taylor approximation gives

$$\varphi_1(V_{in}) \cong \frac{2\pi \Delta \ell}{\lambda_o^2} (\lambda_o - \eta V_{in}). \quad (3.24)$$

The DC terms of (3.24) are neglected since only incremental phase, $\Delta\varphi_1$, is of interest, thereby leading to

$$\mathbf{G}_1 \triangleq \frac{\Delta\varphi_1}{V_{in}} = \frac{-2\pi \Delta \ell \eta}{\lambda_o^2}. \quad (3.25)$$

3.2.2 Feedback loop

The phase modulator and amplifier gain stage are modeled within the feedback loop as \mathbf{G}_3 . Note that φ_2 contains no DC component. It is evident from (3.22) that

$$\mathbf{G}_3 \triangleq \frac{\varphi_2}{V_{out}} = A \frac{\pi}{v_\pi}. \quad (3.26)$$

3.2.3 Interferometric combining and loop filter

The MZI sinusoidal transfer characteristic (2.23) can be rewritten as is a function of $(\varphi_1 + \varphi_2)$:

$$P_{out} = \frac{P_{in}}{2} (1 + \cos(\varphi_1 + \varphi_2)) \quad (3.27)$$

The phase of (3.27) is maintained near $\frac{\pi}{2}$ because the loop filter nulls the error between the half-power reference signal (scaled by the fiber to fiber insertion loss t_{ff}) and the MZI output. When the loop is closed,

$$\varphi_1 + \varphi_2 = \Delta\varphi_1 + \varphi_2 + \frac{\pi}{2}, \quad (3.28)$$

where the variables on the right represent incremental small-signal quantities only. This substitution allows us to rewrite (3.27) as

$$P_{out} = \frac{P_{in}}{2} (1 - \sin(\Delta\varphi_1 + \varphi_2)). \quad (3.29)$$

A first order Taylor expansion about $(\Delta\varphi_1 + \varphi_2) = 0$ is then made, resulting in

$$P_{out} \cong \frac{P_{in}}{2} (1 - (\Delta\varphi_1 + \varphi_2)). \quad (3.30)$$

The DC terms from (3.30) are eliminated to reveal the small signal model for the intensity:

$$\Delta P_{out} = -\frac{P_{in}}{2} (\Delta\varphi_1 + \varphi_2). \quad (3.31)$$

The incremental intensity ΔP_{out} relates to V_{out} through the forward path shown in Figure 3-5. The forward path incorporates the MZI optical loss, detector responsivity, and

integrating loop filter into the model, leading us to the following expression for \mathbf{G}_2 :

$$\mathbf{G}_2 \triangleq \frac{V_{out}}{\Delta\varphi_1 + \varphi_2} = -\frac{t_{ff}P_{in}\mathcal{R}}{2}\mathcal{Z}(s) \quad (3.32)$$

The loop filter used is the same as in (3.18).

3.2.4 Gain Result

The total gain for the Phase Model feedback system in Figure 3-5 is given by

$$g_v = \frac{\mathbf{G}_1\mathbf{G}_2}{1+\mathbf{G}_2\mathbf{G}_3} \quad (3.33)$$

$$g_v = \frac{t_{ff}\mathcal{R}P_{in}\Delta\ell\eta\frac{\pi}{\lambda_0^2}\mathcal{Z}(s)}{1-\frac{t_{ff}A\mathcal{R}P_{in}\mathcal{Z}(s)\pi}{2V_\pi}} \quad (3.34)$$

The Phase Model gain in (3.34) is identical to the result (3.17) obtained from the Intensity Model, verifying that the two models are the same. The primary difference between the two model approaches is that phase model explicitly fixes the argument of the sinusoidal transfer function (2.23) to $\pi/2$, while the intensity Model, on the other hand, fixes the electrode voltage \mathbf{V}_o to $V_\pi/2$ but allows other parameters to vary. For both models the individual link components are characterized the same, so the models give the same result. A plot of the frequency response of (3.34) is identical to the plot in Figure 3-4 for the Intensity Model. A plot of (3.34) versus $\Delta\ell$ can also be seen from the Intensity Model plot in Figure 3-3.

3.3 Dynamic Range

The analysis for dynamic range is approached similarly to the gain analysis. The expressions (3.13) and (3.4) are used to obtain

$$V_o + v_o = t_{ff}\mathcal{R}\mathcal{Z}(s)\Delta P_{out} \quad (3.35)$$

$$= t_{ff}\mathcal{R}\mathcal{Z}(s)\frac{P_{in}}{2} \cos\left(\frac{\pi\mathbf{V}_o\lambda_0}{V_\pi(\lambda_0+\eta\mathbf{V}_i)} + \frac{2\pi\Delta\ell}{\lambda_0+\eta\mathbf{V}_i}\right). \quad (3.36)$$

The quantity $V_o + v_o$ is as defined in (3.2).

Deriving the dynamic range involves expressing v_o as a rational function of v_i and determining how different frequency tones at the input produce mixing at the output. The

system in (3.36) is highly nonlinear in both v_o and v_i , so we must somehow expand the function in a Taylor series manner about both variables. This expansion is similar to above but now expansion must be performed beyond the linear terms to determine nonlinear interactions. Ideally a rational solution to the function of the form (3.37) is desired. (This is a small-signal model, so all DC terms are ignored. Also recall that quiescent points for \mathbf{V}_o and \mathbf{V}_i are $V_\pi/2$ and 0, respectively.)

$$V_o+v_o = \mathcal{RZ}(s) \left(v_o \frac{\partial f}{\partial \mathbf{V}_o} + \frac{v_o^2}{2!} \frac{\partial^2 f}{\partial \mathbf{V}_o^2} + \frac{v_o^3}{3!} \frac{\partial^3 f}{\partial \mathbf{V}_o^3} + \dots + v_i \frac{\partial f}{\partial \mathbf{V}_i} + \frac{v_i^2}{2!} \frac{\partial^2 f}{\partial \mathbf{V}_i^2} + \frac{v_i^3}{3!} \frac{\partial^3 f}{\partial \mathbf{V}_i^3} + \dots \right) \quad (3.37)$$

Evaluation of (3.37) is achievable however solving for the roots of v_o is cumbersome if not impossible for arbitrary orders of the series expansion. Investigation found that the second and higher order terms in $\frac{\partial}{\partial \mathbf{V}_o}$ were small compared to the linear V_{out} term and to the V_{in} terms. To keep the analysis simple, the higher order terms for v_o in (3.37) are neglected. In the expansion for v_{in} , terms above the third order are also insignificant and therefore omitted. These approximations allow for a simple solution for v_o from (3.37). The solution for v_o is shown directly below, where the derivatives have been evaluate at the quiescent points.²

$$v_{out} \cong \alpha \frac{\pi \Delta \ell \eta}{\lambda_o^2} \cos \left(\frac{2\pi \Delta \ell}{\lambda_o} \right) v_{in} + \quad (3.38)$$

$$\alpha \left[\left(\frac{\pi \Delta \ell \eta}{\lambda_o^2} \right)^2 \sin \left(\frac{2\pi \Delta \ell}{\lambda_o} \right) - \frac{\pi \Delta \ell \eta^2}{\lambda_o^3} \cos \left(\frac{2\pi \Delta \ell}{\lambda_o} \right) \right] v_{in}^2 + \quad (3.39)$$

$$\alpha \left[-2 \frac{\pi^2 \Delta \ell^2 \eta^3}{\lambda_o^5} \sin \left(\frac{2\pi \Delta \ell}{\lambda_o} \right) + \frac{\pi \Delta \ell \eta^3}{\lambda_o^4} \cos \left(\frac{2\pi \Delta \ell}{\lambda_o} \right) - \frac{2\pi^3 \Delta \ell^3 \eta^3}{3\lambda_o^6} \cos \left(\frac{2\pi \Delta \ell}{\lambda_o} \right) \right] v_{in}^3 \quad (3.40)$$

The substitution (3.41) is used for α .

$$\alpha \triangleq \mathcal{RZ}(s) P_{in} \quad (3.41)$$

The input voltage is now expressed as a sum of two single frequency tones as in (3.42),

²The derivatives are calculated using the diff function in MAPLE.

substitute this into (3.40), and expand the result trigonometrically.

$$v_{in} = v_o \cos(\omega_1 t) + v_o \cos(\omega_2 t) \quad (3.42)$$

From here the analysis gets complicated to do by hand so MAPLE takes over. The MAPLE script used for this analysis may be referenced in Appendix E.3.

Terms of v_{out} with equivalent frequency components are grouped together, with the linear terms containing $e^{\pm j\omega_1 t}$, the third-order terms containing $e^{\pm j(2\omega_1 - \omega_2)}$, etc. Other significant nonlinearities (*e.g.*, second order) are neglected because a suboctave, bandpassed system is assumed.

Once MAPLE performs the symbolic manipulation, F_1 and F_3 are designated as the coefficients of the first the third order outputs, respectively.

Next the link's Noise Floor (N_{floor}) is calculated to determine the smallest detectable output signal. This involves analyzing the receiver configuration. RIN is canceled by the dual-detector receiver, so the primary noise sources under consideration are shot noise and thermal noise. The shot noise is a Poisson process and the two detectors are uncorrelated so the mean-square shot noise current is given by

$$N_{shot} = \langle i_{shot}^2 \rangle R_{out} = 2qI_{DC}\Delta f R_{out}, \quad (3.43)$$

where Δf is the measurement bandwidth. I_{DC} represents the DC photocurrent in the receiver, which is the current i_1 or i_2 shown in Figure 2-11. Thermal noise is always present at both the input and output, so any gain in the link amplifies this noise. The voltage gain, g_v , arrived at in (3.34) is used to express the output power thermal noise as,

$$N_{thermal} = kT\Delta f + kT|g_v|^2\Delta f. \quad (3.44)$$

For a 1 Hz bandwidth ($\Delta f = 1$ Hz), the power noise floor becomes

$$N_{floor} = kT + kT|g_v|^2 + 2qI_{DC}R_{out} \quad (3.45)$$

where it is assumed that the output resistance, R_{out} , is 50 Ω .

The gain in (3.17) is substituted in the NF expression (3.45) using the transimpedance

Table 3.1: Table of link parameter numerical values.

Link Parameter	Value	Units
λ_o	1.064	μm
η	$5.7 \cdot 10^{-14}$	m/V
I_{DC}	.500	mA
v_π	6	V
\mathbf{V}_o	2.5	V
P_{in}	4	mW
t_{ff}	.25	dimensionless
\mathcal{R}	.40	A/W
R_1	330	Ω
R_2	330	Ω
A	100	dimensionless

loop filter $\mathcal{Z}(s)$ expression defined in (3.18) and setting $R_1 = R_2$.

The frequency-dependent noise floor is found to be

$$N_{floor} = kT + kT \left| \frac{t_{ff} \mathcal{R} P_{in} \Delta \ell \eta \frac{\pi}{\omega C \lambda_o^2}}{1 + j \frac{t_{ff} A \mathcal{R} P_{in} \pi}{2 V_\pi \omega C}} \right|^2 + 100qI_{DC}. \quad (3.46)$$

A Bode plot of the noise floor at 1 MHz is shown in Figure 3-6 using the link parameter values given in Table 3.1.

Once the noise floor is obtained, MAPLE is used to solve for the x-intercept value (in Volts) where F_3 intersects the N_{floor} .

$$v_{suppr} \triangleq x = (\text{solve}(N_{floor} = F_3^2/50, nu)[1]); \quad (3.47)$$

This generates a cumbersome nonlinear function of $\Delta \ell$ that shrinks with growing $\Delta \ell$. The x-intercept is denoted as v_{suppr} because it is the input voltage that suppresses F_3 to the noise floor. The first order output $F_1(v_{suppr})$ is evaluated at the suppression input level.

The SFDR is determined by the height above the noise floor in dB of the first order output at the suppression input. So,

$$SFDR = 10 \log_{10} \left(1000 |F_1(v_{suppr})|^2 / 50 \right) - 10 \log_{10} |1000 N_{floor}|. \quad (3.48)$$

The result is plotted in Figures 3-7 and 3-8, which both show an inverse relationship between

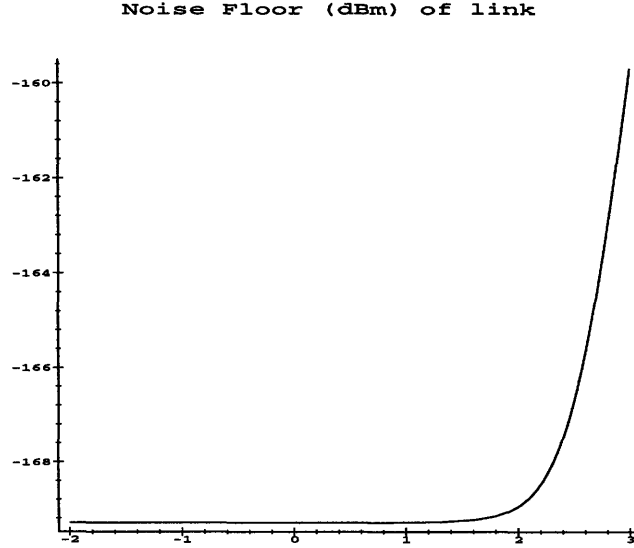


Figure 3-6: Noise floor (dBm) plotted versus $\log_{10} \Delta\ell$ at 1 MHz using given link parameters.

dynamic range and $\Delta\ell$. Note that these two plots have different y-axes, so the discontinuity is artificial.

3.4 Noise Figure

The noise figure is a measure of the degradation of the signal to noise ratio (SNR) between the input to the output of a link. It is defined as follows.

$$NF \triangleq \frac{SNR_{in}}{SNR_{out}} \quad (3.49)$$

$$= \frac{N_{out}}{N_{in}|g_v|^2} \quad (3.50)$$

$$(3.51)$$

The parameter g_v is small-signal voltage gain as defined earlier.

To determine noise figure (NF) the principal noise sources are again assumed to be thermal noise and detector shot noise, as discussed above in Section 3.3. Frequency noise on the laser and thermal expansion/contraction in the fiber interferometer are both neglected.

SFDR (1 Hz bw) over range .01064m - 1.064m

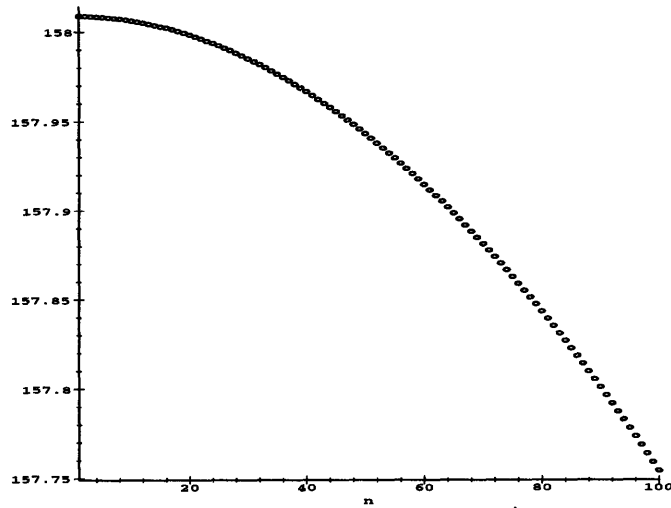


Figure 3-7: Spurious Free Dynamic Range ($\text{dB} \times \text{Hz}^{2/3}$) plotted versus $n = \frac{\Delta\ell}{1.064 \text{ cm}}$ varying from 1 to 100, or .01064 m to 1.064 m. The horizontal $\Delta\ell$ axis is plotted linearly. This plot exaggerates SFDR variation over given range; note vertical axis labels.

SFDR (1 Hz bw) over range 1.064m - 106.4m

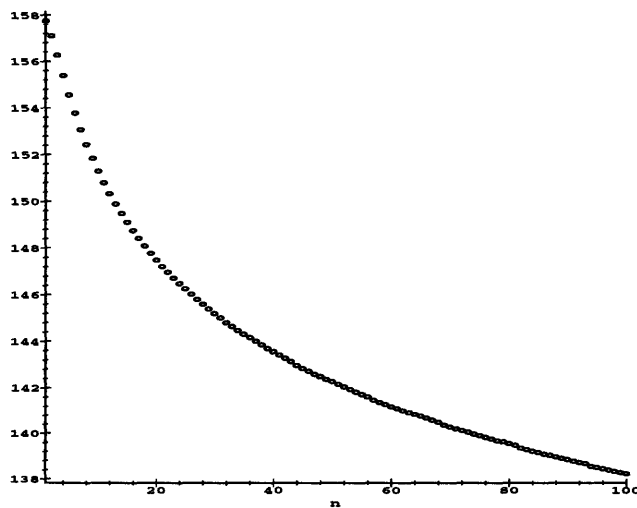


Figure 3-8: Spurious Free Dynamic Range ($\text{dB} \times \text{Hz}^{2/3}$) plotted versus $n = \frac{\Delta\ell}{1.064 \text{ m}}$ varying from 1 to 100, or 1.064 m to 106.4 m. The horizontal $\Delta\ell$ axis is plotted linearly.

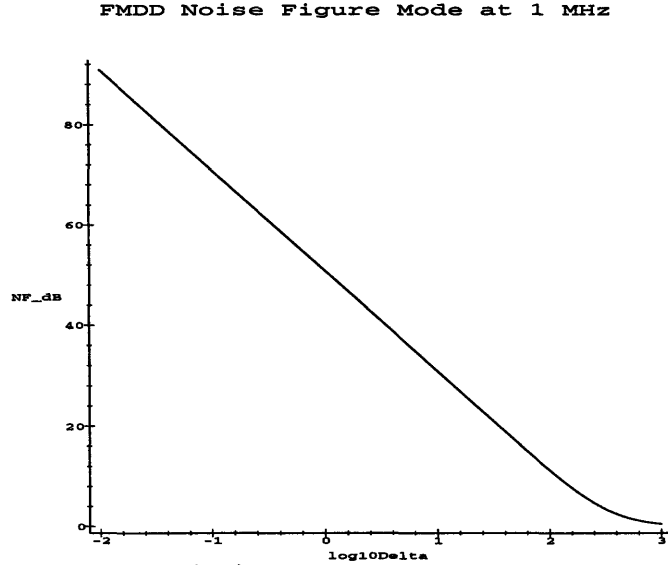


Figure 3-9: Noise figure (dB) model plotted versus $\log_{10} \Delta \ell$ (referenced to 1 m) using parameters in Table 3-1. Plotted at 1 MHz.

The noise figure in (3.51) can be expressed as

$$NF = \frac{N_{floor}}{kT|g_v|^2}, \quad (3.52)$$

where N_{floor} has the same formulation as in (3.46). Evaluation of (3.52) is done by substituting in (3.46) and (3.17) and using the parameter values in Table 3.1. The result is plotted at 1 MHz versus $10 \log_{10}(\Delta \ell)$ in Figure 3-9. Notice that the noise figure improves as $\Delta \ell$ increases, due to the likewise improvement in gain.

A slightly modified version of a noise figure expression that uses the same noise considerations found in [26] is shown below in (3.53).

$$NF = 10 \log_{10} \left(1 + \frac{qR_D \mathcal{R} t_{ff} P_{in}}{kT|g_v|^2} + \frac{1}{|g_v|^2} \right) \quad (3.53)$$

This general expression (3.53) is plotted together with (3.51) in Figure 3-10 to show that the two behave similarly with increasing $\Delta \ell$.

FMDD Noise Figure Model and CHC Noise Figure Model (dB)

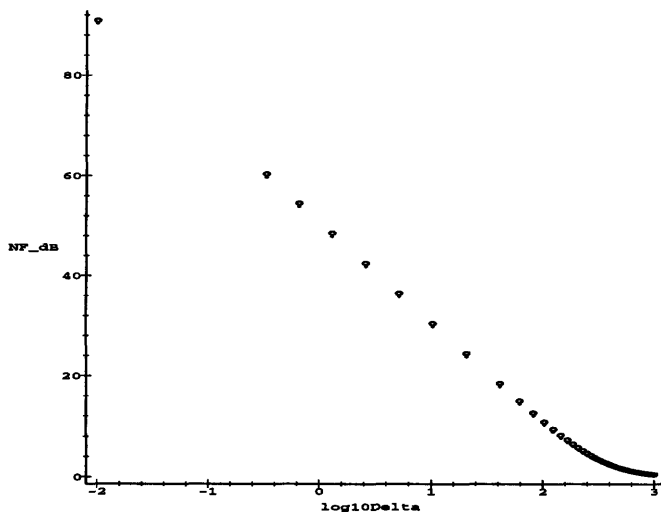


Figure 3-10: FMDD noise figure model and modified Cox noise figure model in [26] plotted together versus $\log_{10} \Delta \ell$ (referenced to 1 m) using parameters in Table 3-1. FMDD model represented with o-marks, while modified noise figure model of Cox represented by x-marks. The models agree perfectly with both showing noise figure improvements with increasing $\Delta \ell$. Plot shown for 1 MHz.

Chapter 4

Experimental Results and Conclusions

4.1 Link Measurements

This section presents measurements taken on the FMDD link and compares them to the models.

4.1.1 Gain

The gain has been measured using the link setup shown in Figure 2-11 and modeled in Section 3.1. Data for a link with a $\Delta\ell$ of 1.080 m is shown in Figure 4-3. The measurement yields a power gain of

$$G = -40 \text{ dB}, \quad (4.1)$$

and a 3 dB bandwidth of

$$f_{3dB} = 6.4 \text{ MHz}. \quad (4.2)$$

The frequency response of the experimental gain is plotted with the theoretical model in Figure 4-1. These measurements have an accuracy of ± 2 dB. The result agrees to within 5 dB of the model.

The free parameters V_π and η are now adjusted within their measurement accuracies to match the data. Table 4.1 outlines the free parameter adjustment. The data perfectly matches the adjusted model, as shown in Figure 4-2. The experimental 3 dB breakpoint

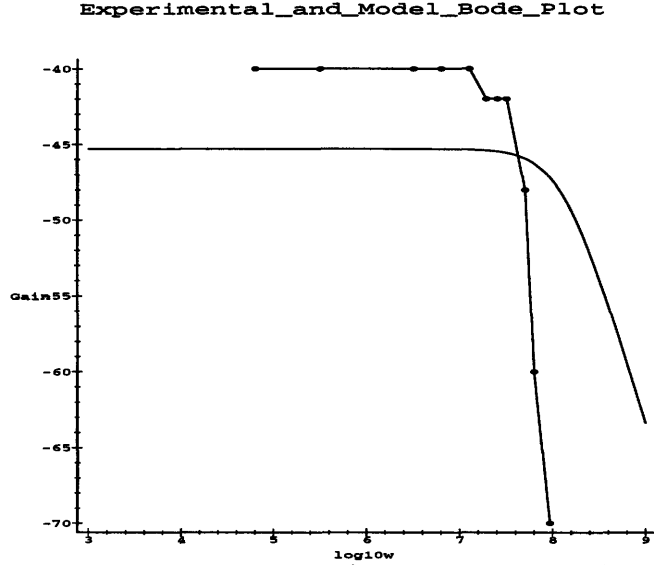


Figure 4-1: Experimental comparison of FMDD gain model and experimental result. The gain in dB is plotted versus $\log_{10}(\frac{\omega}{1 \text{ rad/sec}})$ at $\Delta\ell = 1$ m. The lower trace is the experimental result at $\Delta\ell = 1.080$ m, while the upper trace is the result previously shown in Figure 3-7. Results agree to within 5 dB at frequencies below the experimental 3 dB breakpoint of $f_{3dB} = 6.4$ MHz. The model f_{3dB} occurs at 20 MHz.

is 6.4 MHz, while the model predicts 20.0 MHz. The model, however, only incorporated the frequency considerations for the integrating Op Amp, so we believe that the breakpoint discrepancy is due to other Op Amps in the loop whose characteristics have not been modeled.

Some options for improving this gain have been investigated, such as increasing the control loop gain A , and increasing the path length difference $\Delta\ell$. There is a tradeoff between A and $\Delta\ell$, however, since large A compromises stability of the loop and large $\Delta\ell$ incurs excessive sensitivity to laser phase noise. Another option which was not explored

Table 4.1: Table of free parameter adjustments.

Link Parameter	Measured Value	Adjusted Value	Units
η	$5.7 \cdot 10^{-14}$	$7.0 \cdot 10^{-14}$	m/V
	(15)	(18)	(MHz/V)
V_{π}	5.0	7.5	V

Experimental_and_Adjusted_Model_Bode_Plot

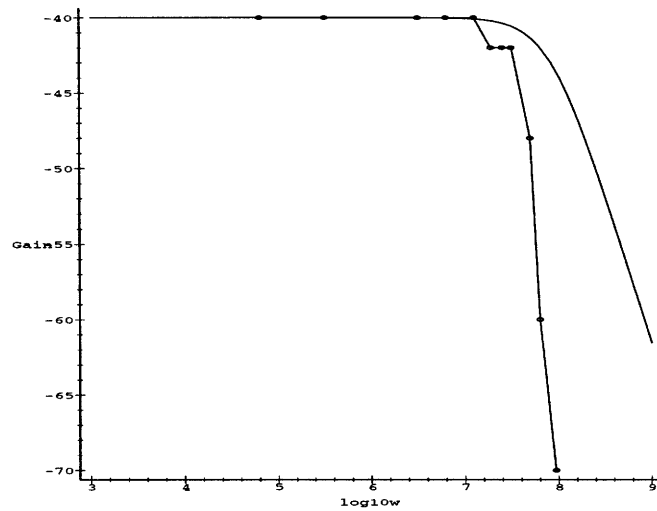


Figure 4-2: Experimental verification of Intensity Model. The gain in dB is plotted versus $\log_{10}(\frac{\omega}{1\text{rad/sec}})$ at $\Delta\ell = 1$ m. The upper trace is the experimental result at $\Delta\ell = 1.080$ m, while the lower trace is the result previously shown in Figure 3-4. Results agree to within 0.5 dB at frequencies below the experimental 3 dB breakpoint of $f_{3dB} = 6.4$ MHz. The model f_{3dB} occurs at 20 MHz. Lower breakpoint and faster rolloff observed in the data are believed to be due to the unmodeled characteristics of the Op Amps.

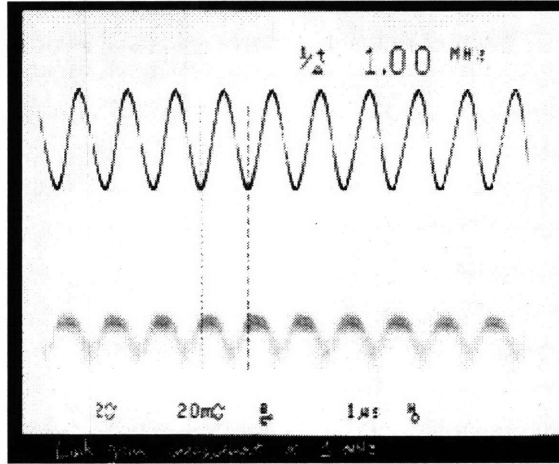


Figure 4-3: Link gain measurement. Time domain response at 1 MHz. The lower trace is the link output at 20 mV peak-to-peak and the upper trace is the link input at 2 V peak-to-peak. The gain in dB is $20 \log_{10}(\frac{20\text{mV}}{2\text{V}}) = -40 \text{ dB}$.

would be to add gain to the forward path.

4.1.2 Noise Figure

The noise figure has been measured at $\Delta\ell = 1.08 \text{ m}$ using the data shown in Figures 4-6 and 4-5. The input signal to noise ratio (SNR_{in}) is 102 dB, and the output signal to noise ratio (SNR_{out}) is 62 dB. The measurement has an accuracy of $\pm 2 \text{ dB}$. Our measurement yields

$$NF = \text{SNR}_{in} - \text{SNR}_{out} = 40 \text{ dB}. \quad (4.3)$$

This is off by -10.2 dB compared to the model shown in Figure 3-9. If the model parameters are readjusted according to Table 4.1, then the experiment matches the model more closely, as shown in Figure 4-4. This corrected model gives $NF = 45.0 \text{ dB}$, which is only off by 5 dB from the measurement. The discrepancy between the experimental result and the model is due to measurement error.

Experimental_and_Adjusted_Model_Noise_Figure

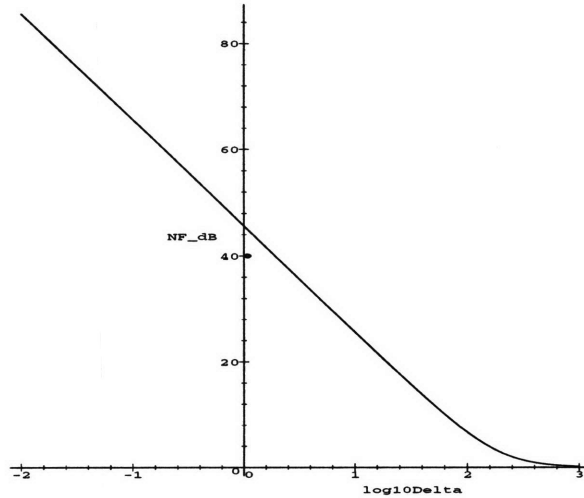


Figure 4-4: Comparison of adjusted noise figure model and experimental result at 1 MHz. The parameters η and V_π were adjusted. The noise figure in dB is plotted versus $\log_{10}(\frac{\Delta\ell}{1m})$. Our experimental yielded $NF = 40$ dB at $\Delta\ell = 1.080$ m, while the model gives 45.0 dB. Discrepancy of 5 dB is likely due to measurement error and modeling.

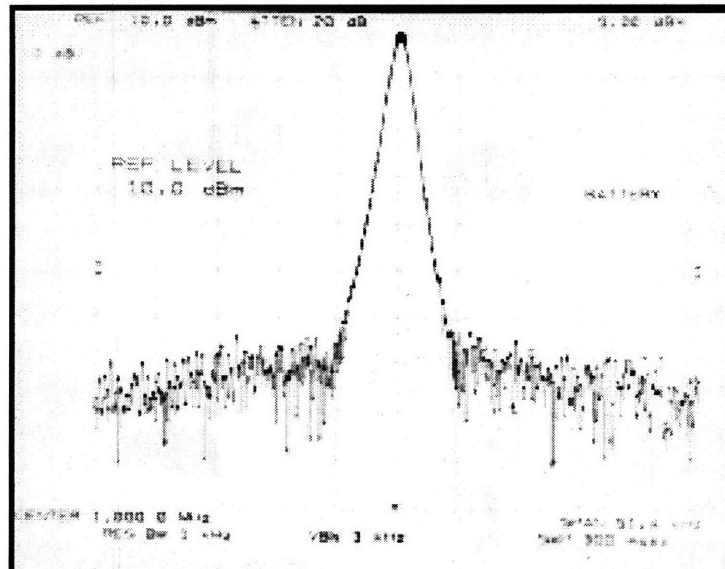


Figure 4-5: Link input spectrum at 1 MHz, viewed over 50 kHz band. Input is 9 dBm measured under 50 Ω load of RF spectrum analyzer. Normal load is ~ 1 M Ω . Noise floor is -93 dBm over a 1 Hz bandwidth. Measurement yields $SNR_{in} = 102$ dB.

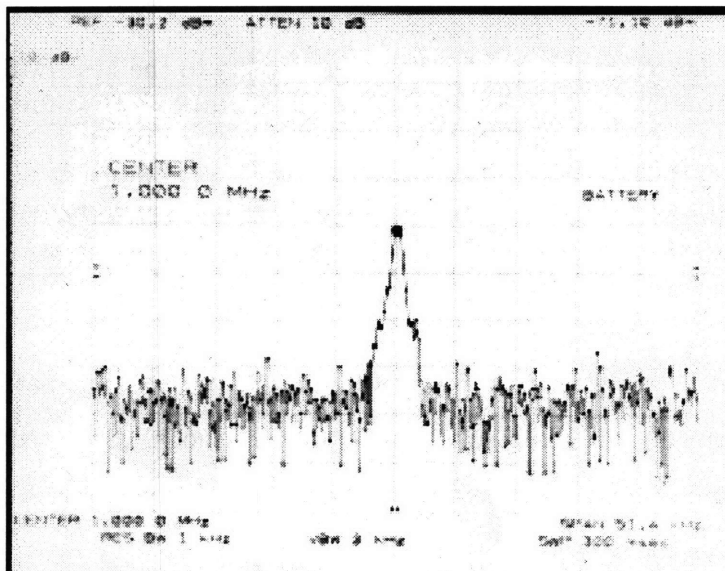


Figure 4-6: Link output spectrum at 1 MHz, viewed over 50 kHz band. Output is at -71 dBm under 50Ω RF spectrum analyzer load; V_{out} is attenuated by .068 through a resistor before being sent to spectrum analyzer low impedance input. Noise floor is -133 dBm over a 1 Hz bandwidth. Measurement yields $SNR_{out} = 62$ dB.

4.1.3 Spurious-Free Dynamic Range

The electrical power supplied from the HA3-5033 to the EO phase modulator's low-impedance input sometimes exceeded the value given in Section 2.2.3. This is believed to have caused the destruction of the wire bond connection in the phase modulator, thereby delaying measurement of the link's dynamic range until after the completion of this thesis.

4.2 Discussion

The demonstration of a prototype FMDD link has allowed verification of theoretical gain and noise figure calculations with experimental results to within 5 dB. The experimental results of the link are displayed in Table 4.2, where they are compared to important figures of merit for state of the art intensity modulated direct detection links. It is feasible that FMDD links will achieve performance comparable to the best IMDD or coherent links at optical powers near 0 dBm if the some problems are successfully addressed.

The gain and noise figure measurements are very close, suggesting that increasing the gain to 0 dB could considerably improve the noise figure. In fact, I realized in retrospect

Table 4.2: Comparison of FMDD link results to the best IMDD links.

Link Parameter	Value for FMDD Link	Value for IMDD Link
Gain (G)	-40 dB	0 dB
Noise Figure (NF)	40 dB	5 dB
Dynamic Range (SFDR)	unavailable	120 dB·Hz ^{2/3}
Optical Power	6 dBm	20 dBm

that adding gain A (see gain expression (3.17)) to the the forward path (\mathbf{H}_2) rather than the feedback path (\mathbf{H}_3), would result in increasing the model gain by 40 dB to yield a gain of 0 dB. This would improve the gain and noise figure, but only at the expense of dynamic range, as is always the case for pre-amplifying.

Several other limitations were encountered on the experimental work for the FMDD link. A major hindrance is laser frequency noise on the source, which translates to intensity noise at the MZI output. Suppression of this noise is highly unpredictable, and measurements can only be taken when the laser achieves decent wavelength stabilization. Unfortunately this process often takes considerable time and is easily disrupted for unknown reasons. One possible solution to this problem is temperature control of the EO tunable DPSSL, which was not implemented in order to maintain simplicity of the design under time constraints. Thermal noise is believed to be another chief problem because the MZI, constructed out of ~ 3 m fiber lengths, is highly susceptible to nanoscale expansions or contractions due to thermal fluctuations. The MZI was insulated as well as possible, but ideally a temperature controller would be used to zero out thermal fluctuations present in the fiber. A better but more involved solution would be to integrate the MZI on an all-LiNbO₃ substrate, making the modulator more rigid and less likely to alter its geometry under thermal fluctuations.

The two noise sources discussed in the above paragraph occur at low frequency, *i.e.*, < 100 kHz. At high frequency one would expect the link to be immune to this noise, however, it is important to realize that this noise can considerably disrupt the DC reference bias point away from the linear operating point on the MZI. This has potentially adverse effects upon dynamic range. It also causes trouble for the loop filter which will integrate up to +5 V or down to -5 V if the DC fluctuation is high enough. Taking data is difficult because I must wait till the loop stabilizes for at least a few moments at the proper bias point.

4.3 Conclusions and Future Work

A novel frequency modulated direct detection link has been successfully designed and built in this thesis. Experimental results show good comparison with modeling for gain and noise figure, while dynamic range will be measured in the future.

This initial investigation of FMDD links will lead to considerable future development that could bring the overall performance of FMDD links closer to that of IMDD links. The improvements discussed in Section 4.2 should be implemented in order to demonstrate the performance improvements in future FMDD links. There are some more significant design changes that could provide additional improvements. Expanding the FM DPSSL's tuning range per unit volt could be accomplished by using electro-optic materials with ferro-elastic or ferro-electric properties [27] or by narrowing the electrode spacing.[27, 28] The linewidth could also be controlled by using stabilization techniques [29] would improve things considerably. New receiver designs could employ simpler or more linear interferometric techniques. Examples include the Michelson interferometer which uses a single arm instead of two, or the half-coupler or linearized Mach-Zehnder interferometers which provide improved linearity over a standard Mach-Zehnder. For a system with expanded tuning range on the FM source, diffraction grating techniques such as a double-pass monochromator [30] could provide high dynamic range interferometry over a large optical bandwidth.

Several improvements could be implemented on the feedback electronics. Currently the receiver attains a bandwidth of about 5 MHz using standard Op Amps and circuit elements. High speed amplifiers could be designed and implemented to carry the link out to 450 MHz where it could be demonstrated in the UHF range. This improvement might involve more sophisticated feedback control circuits, such as the second-order loop discussed in Appendix C. Impedance matching could also be performed to run all electronics in low-impedance state to match properly to the electro-optical devices. This would avoid problems encountered with using high-impedance electronics to drive the low-impedance phase modulator. Finally, integration of the photodetectors into a monolithic device could enable the link operate at even higher frequencies, since the dual-detector receiver currently is bandwidth limited to about 500 MHz.

In summary, this work has been extremely fulfilling and rewarding. I am excited to be part of an effort at Lincoln Laboratory to forge new ground in the efforts of FMDD links

and I look forward to seeing further developments in the near future that will make these novel links an attractive alternative to IMDD analog links. The wide range of disciplines that this thesis project entailed has allowed me to develop much stronger skills in free-space optical design, electro-optics, analog circuit design, and feedback control. I look forward to applying this knowledge to my research pursuits in my Ph.D studies and beyond.

Appendix A

Free-Space Source-to-Fiber Design

Coupling the free space laser output into fiber involves properly collimating the beam and then refocusing it onto the fiber core. The 3 dB couplers are constructed of polarization maintaining (PM) fiber which preserve the initial linear polarization through the coupler so that the light enters the electro-optic phase modulator polarized along the correct axis.

Coupling into the HB1000 PM fiber also requires orienting the fiber at the correct angle so that the linear polarized light from the laser is launched into the proper axis (*i.e.*, fast or slow) of the fiber. In addition to rotational alignment, the focused spot size must match the 6 μm mode size of the fiber. The focusing lenses must also be chosen to appropriately match the numerical aperture (NA) of the fiber also in order to contain the light within the core of the fiber.

A.1 Background

The lens problem of collimating and coupling the beam is approached using Gaussian optics. The two fundamental equations for Gaussian beams describe how the laser spot size and radius of curvature vary over distance.

$$R(z) = z \left[1 + \left(\frac{\pi w_o^2}{\lambda z} \right)^2 \right] \quad (\text{A.1})$$

$$w(z) = w_o \left[1 + \left(\frac{\lambda z}{\pi w_o^2} \right)^2 \right]^{1/2} \quad (\text{A.2})$$

It is useful to define the *q-parameter* as follows:

$$\frac{1}{q} \triangleq \frac{1}{R(z)} - j \frac{\lambda}{\pi w^2(z)} \quad (\text{A.3})$$

From *q* the two important parameters spot size and radius of curvature can be determined.

A matrix formalism discussed in [31] will be used in this analysis. As a beam propagates through distances, lenses, and mirrors, the initial q_o undergoes a series of transformations each representable by a matrix. The total transformation can be represented in a simple manner by one matrix, *M*, (A.4). This matrix modifies q_o in the following manner.

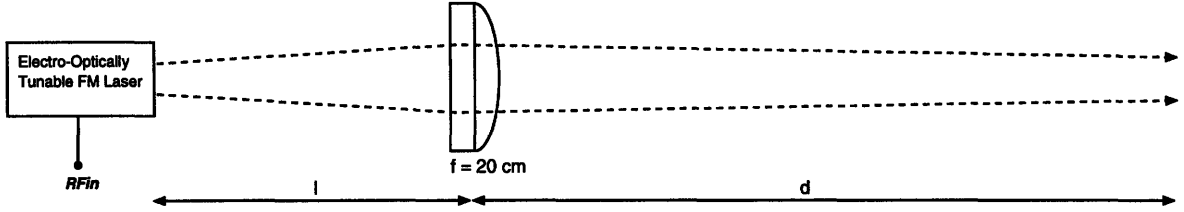


Figure A-1: Free-space beam collimation setup using single plano-convex lens.

$$M = \begin{bmatrix} A & B \\ C & D \end{bmatrix}, \quad q = \frac{Aq_o + B}{Cq_o + D} \quad (\text{A.4})$$

A.2 Collimation

It is evident from Equations A.1 and A.2 that all Gaussian beams eventually acquire divergence over distance. Although perfect collimation is impossible in our setup, closely ideal beam characteristics may be achieved provided that all propagation distances are short. The simplest approach is to use a single lens, as illustrated in Figure A-1, that gives a fairly tight beam over a few meters. Since the output of the laser diverges slowly, a slow lens with a 20 cm focal length is chosen.

This setup is modeled using the matrix formalism. For a free space distance, l , the transformation matrix for q is given by,

$$M = \begin{bmatrix} 1 & l \\ 0 & 1 \end{bmatrix}. \quad (\text{A.5})$$

Similarly, for a lens of focal length f , the transformation matrix is,

$$M = \begin{bmatrix} 1 & 0 \\ -1/f & 1 \end{bmatrix}. \quad (\text{A.6})$$

To determine the waist size as a function of l and d (see Figure A-1), just multiply the matrices and solve for $w(z)$. The optimal lens position can be determined from Figure A-2, which is a 3D plot of the waist size versus l and d . The result matches intuition to place the lens near its focal length to get the best collimation. With the lens placed at 21 cm, the Gaussian beam behaves nearly collimated over a couple of meters as shown in the plot of Figure A-3.

A.3 PM Fiber Coupling

Single mode fiber couplers are composed of a fiber positioner and a microscope objective, both of which can be finely positioned. The objective is chosen to match the numerical aperture (NA) of the fiber so that the focused light converges at the proper angle into the

Waist size (m) vs. l (m) and d (m)

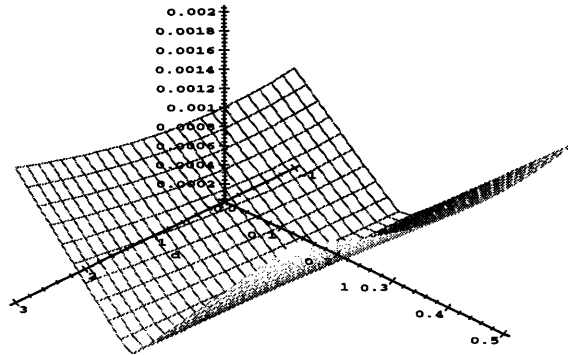


Figure A-2: Waist size in meters for $f = 20$ cm lens.

Waist size (m) vs. d at $l=0.21$

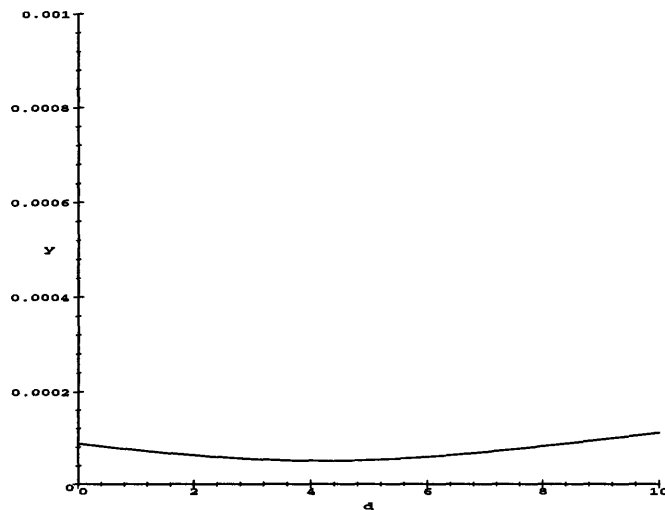


Figure A-3: Waist size in meters for $f = 20$ cm lens and $l = 21$ cm lens position.

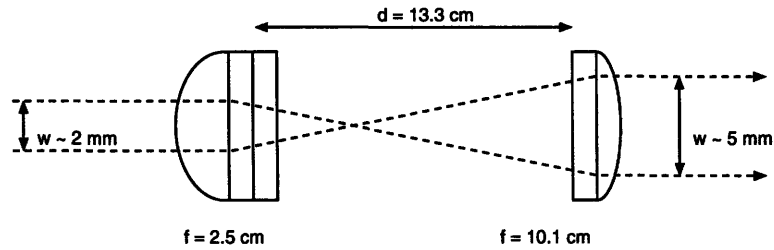


Figure A-4: Free-space beam expander setup using single plano-convex lenses.

core of the fiber. For efficient coupling, the incident beam is mode-matched to the objective by controlling the beam waist size. The relationship between the beam waist diameter (D), the focal length (f), the light wavelength (λ), and the fiber mode size (w) is described by (A.7).

$$f = D \left(\frac{\pi w}{4\lambda} \right) \quad (\text{A.7})$$

To couple into the 3dB-coupler's single-mode PM fiber with NA of 0.1, an 5X, .10 NA objective is needed. The 5X objective used has a focal length of 25.5 mm. The fiber mode size is $6 \mu\text{m}$ and the wavelength is $1.064 \mu\text{m}$. From (A.7), the necessary beam waist diameter at the input of the objective is $D = 5.8\text{mm}$.

The output waist size from the collimating lens is about 2 mm in diameter, so to properly mode match to the objective the beam size must be readjusted. This is a problem in general for single mode fibers with small NAs, however, it can be overcome with the use of a beam expander.

A.3.1 Beam Expander

The beam expander is a simple technique used to adjust beam diameters. Two lenses are placed at their focal lengths from a set point. Assuming the input beam is closely collimated, the fast lens will focus to a spot and then the slower lens will recollimate the beam after it has acquired more divergence. Figure A-4 shows a diagram of a beam expander.

The magnification of the beam expander is given by the ratio of the lens focal lengths,

$$m = \frac{f_{out}}{f_{in}}. \quad (\text{A.8})$$

Using 38 mm and 100 mm focal lengths for the input and output lenses, respectively, gives a magnification of $m \approx 2.7$. As shown in Figure A-4, this provides an output waist size of approximately 5 mm, which is the required diameter for the 5X coupling objective.

A.3.2 Improvements

Coupling without a beam expander to properly mode match the the low-power objective gave optical coupling efficiency of about 10 %. Using a beam expander, the coupling efficiency was improved to almost 40 %.

Appendix B

Free-Space Source Considerations

Practical considerations that are easily implemented in all-fiber based systems become more difficult to address in prototype links that operate partially or wholly in free-space. These issues include isolation, polarization control, and scattering. To successfully operate the free-space optical FM transmitter, several systems in bulk optics have been implemented.

B.1 Link Transmitter

A diagram in Figure B-1 shows the components used in the laser transmitter. An isolator is inserted between the laser and the other optics. This prevents back reflection from non-ideally coated mirrors and lenses by using a polarizing beamsplitter (PBS) and two quarter wave plates (QWP). The QWPs rotate the polarization from linear to circular, so that reflections are converted to a polarization orthogonal to the laser's output. The polarizing beamsplitter dumps this unwanted light before it reenters the laser cavity. Most of the backreflection is due to a SuperCavity Fabry-Perot cavity installed in the setup. The high finesse of the cavity demands the need of an isolator.

A dielectric (*i.e.*, polarization sensitive) beamsplitter is used to couple a small percentage of the light into the SuperCavity. The PM fiber on the 3 dB coupler is also polarization sensitive. This requires that the quarter wave plates and PBS be accurately aligned to provide the correct polarization.

The optics are anti-reflection coated (broadband or narrowband) for 1.064 μm radiation. This includes the beamsplitter, lenses, QWPs, and objectives.

Add dimensions to Figure B-1.

B.2 Link Photo

A scanned photo showing all of the link transmitter and part of the receiver is shown in Figure B-2.

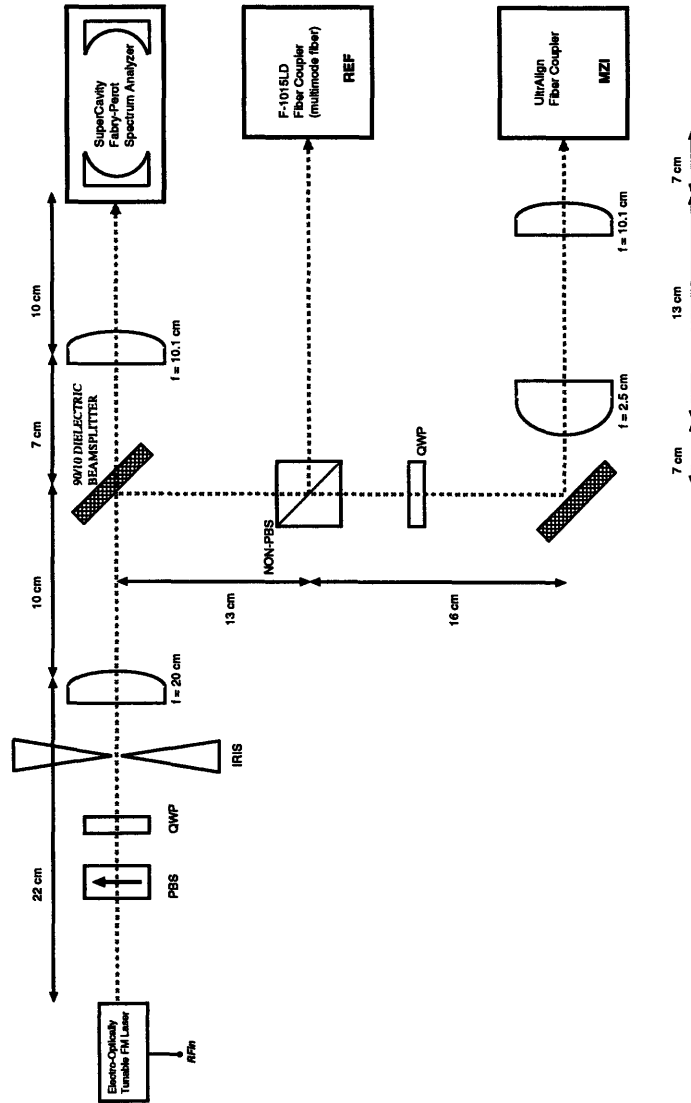


Figure B-1: Free-space optical transmitter for FMDD link.

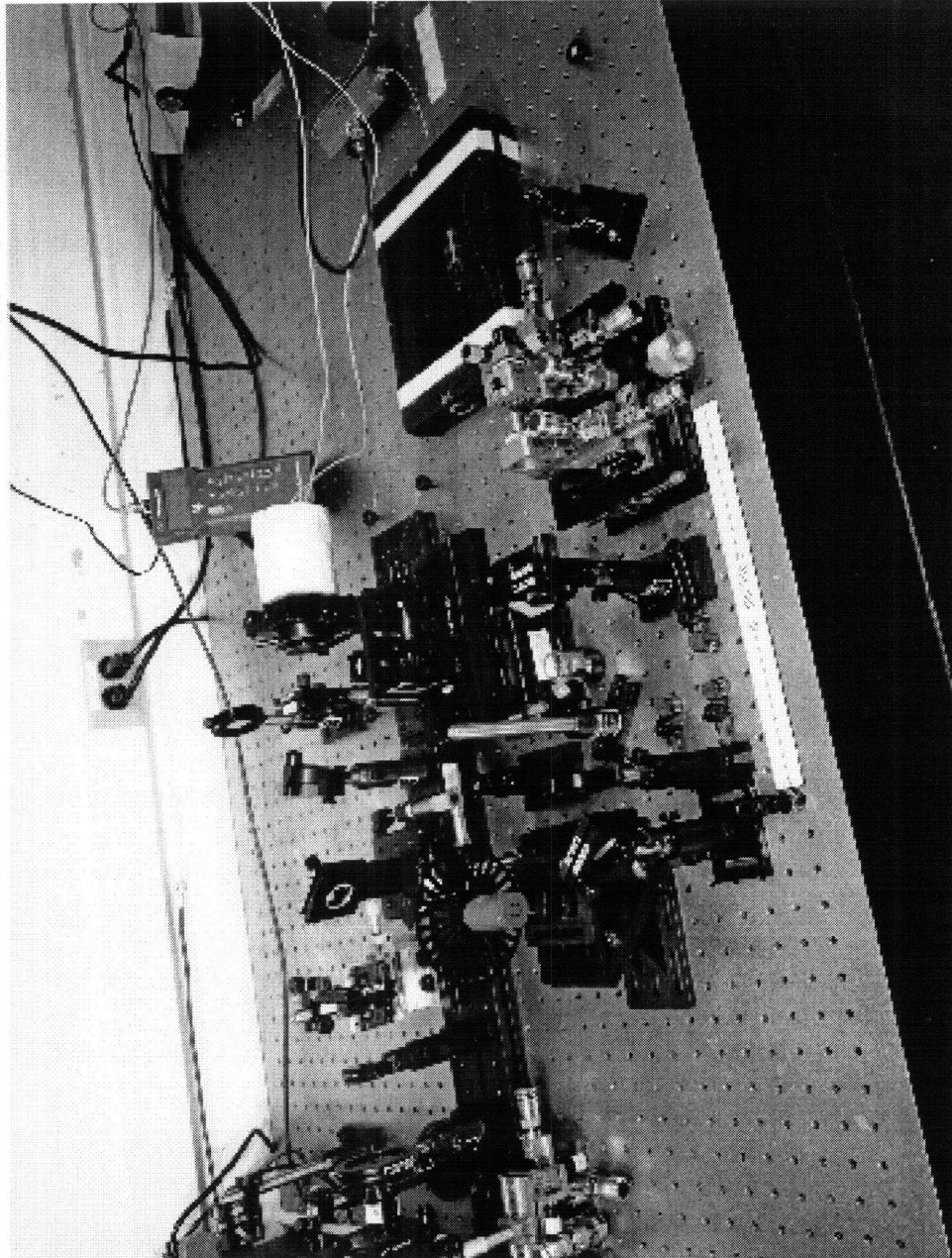


Figure B-2: Photo of free-space portion of optical FMDD link including the 3dB coupler and phase modulator of the fiber-based receiver.

Appendix C

Feedback Loop Analysis

C.1 First order loop

The general gain model expression in (3.16) is helpful for understanding the behavior of the feedback loop. The loop filter represented by $\mathbf{H}_2(s)$ is some sort of integrator exhibiting rolloff with frequency. The $1/s$ or $1/s^2$ behavior is necessary to maintain stability in the feedback loop, but such rolloff should not degrade the gain.

The advantage of feedback comes into play when

$$\mathbf{H}_2\mathbf{H}_3 \gg 1, \quad (\text{C.1})$$

because then (3.16) reduces to

$$g_v \approx \frac{\mathbf{H}_1}{\mathbf{H}_3}. \quad (\text{C.2})$$

The loop filter no longer affects the bandwidth of the gain when the above feedback condition (C.1) holds. This explains the flat behavior in the gain below the breakpoint in Figure 3-3.

In order to achieve condition (C.1), high performance amplifiers or choosing $R_1 > R_2$ could be used to increase \mathbf{H}_2 . It is simpler, however, just to add amplification A to the feedback \mathbf{H}_3 , as represented in Section 2.2.3 and (3.14) and set $R_1 = R_2$. The parameter K_o from (3.14) is measured and calculated to be $\approx .001$ amperes, so for $A = 1$ the loop 3 dB bandwidth is only 160 kHz. A 3 dB bandwidth of 16 MHz, which enables measurements to be taken considerably above thermal noise, is achieved by adding amplification of $A = 100$ to \mathbf{H}_3 .

C.2 Second order loop overview

A second-order loop filter could be also be used to satisfy (C.1). A second-order integrator has the transfer function

$$H(s) = -\frac{1 + R_2(C_1 + C_2)}{R_1 R_2 C_1 C_2}. \quad (\text{C.3})$$

The circuit is shown in Figure C-1, and the Bode plot is shown in Figure C-2. Below the breakpoint of $\omega = \frac{1}{R_2(C_1 + C_2)}$, the loop falls off as $1/s^2$. After the breakpoint, the behavior is $1/s$. This integrator still crosses over at 0 dB at the same frequency as a first-order integrator would, but it provides higher gain at low frequencies.

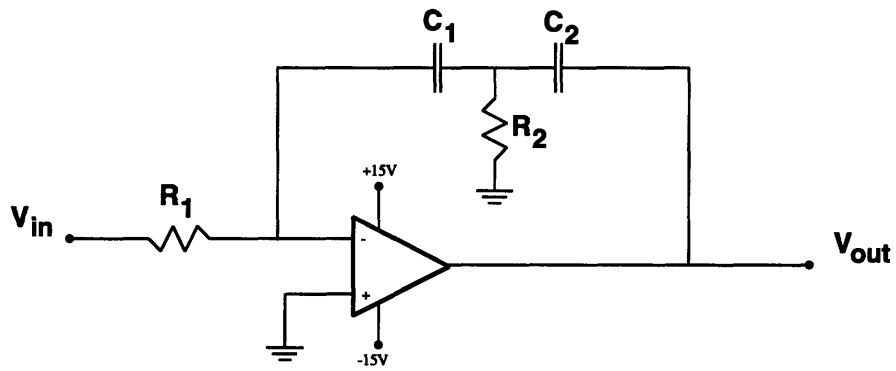


Figure C-1: Second-Order Integrator.

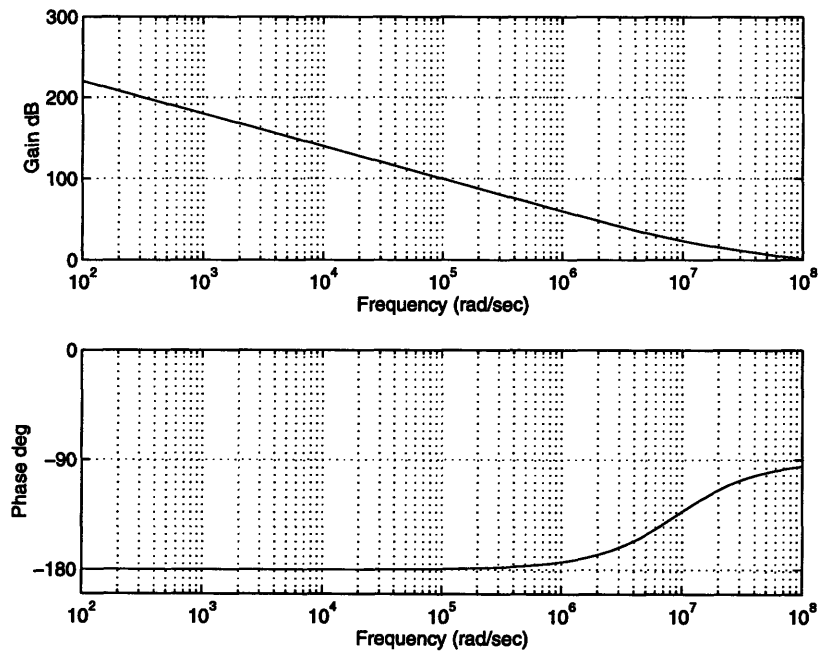


Figure C-2: Second-Order Integrator Bode Plot with $C_1 = 100 \text{ pF}$, $C_2 = 1000 \text{ pF}$, $R_1 = R_2 = 100 \text{ }\Omega$.

Appendix D

Dual-Detector Balanced Receiver

A diagram of the dual-detector receiver assembly is displayed in Figure D-1. The photodetectors are placed near each other to maximize the bandwidth of the receiver. The SMA connector output is wired to the midpoint of the photodetectors to measure the difference current.

Figure D-2 shows the circuit schematic for the photodetectors. The capacitors provide an RF path to ground for the diodes when they are DC reverse biased. This parallel capacitor combination nulls out higher order effects in the capacitors at high frequency to maintain a broadband RF path.

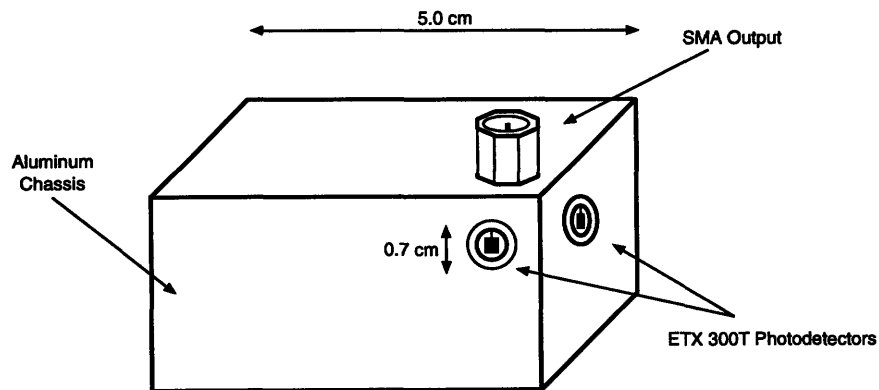


Figure D-1: Drawing of dual-detector balanced receiver assembly.

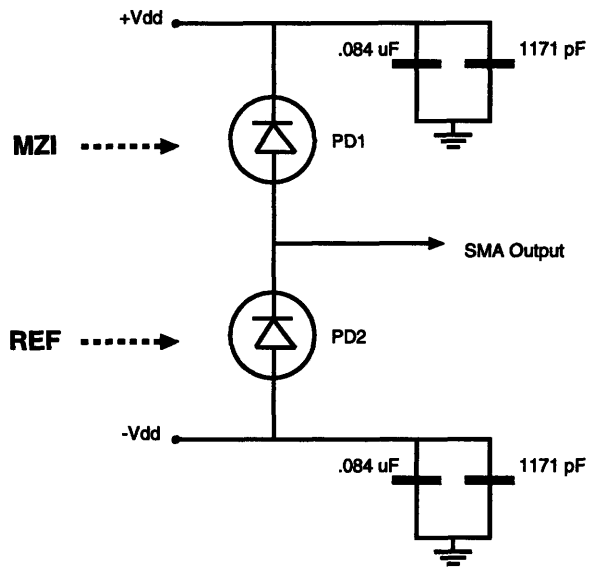


Figure D-2: Schematic of dual-detector balanced receiver circuit. Detectors are Epitaxx ETX300T InGaAs Photodetectors.

Appendix E

MAPLE Scripts

The scripts designed to model the link in MAPLE¹ are included in this Appendix.

E.1 Gain Analysis - Intensity Model

Script file `gain-feedback.ms`.

```
> ### Intensity Gain Model: 1st order linear feedback analysis -
JMR, March '97
> restart;
-----
> # Neglect cos(Delta) terms since they disrupt the phase of the
> # transfer characteristic from Pi/2 when Delta is not integral
> # number of wavelengths
> ###Ki :=
(1/2*Ii*sin((Pi*lambda[o]/2+2*Pi*Delta)/lambda[o])*Pi*
(lambda[o]/2+2*Delta)/lambda[o]^2*eta);
> Ki := (1/2*Ii*Pi*(lambda[o]/2+2*Delta)/lambda[o]^2*eta)
-----
> ###Ko := -Ii*Pi/(2*v[pi])*sin(Pi/2 + 2*Pi*Delta/lambda[o]);
> Ko := -Ii*Pi/(2*v[pi])
> Z := 1/(sqrt(-1)*omega*C)
> # Assume forward path is tff*R*Z(s):
> gv := (tff*R*Ki*Z)/(1 + tff*A*R*Ko*Z)
>
>
> # above equation in MAPLE format
> #####-1/2*I*tff*R*Ii*sin((1/2*Pi*lambda[o]+2*Pi*Delta)/lambda[o])*
Pi*(1/2*lambda[o]+2*Delta)/lambda[o]^2*eta/omega/C/
(1+1/2*I*tff*R*Ii*Pi/v[pi]*cos(2*Pi*Delta/lambda[o])/omega/C)\
>
> ###lambda[o] := 1.064*10^(-6); eta :=7*10^(-14); evalf(Pi);
v[pi] :=7.5; Vo := 3.75; Ii := .004; tff := 0.25; R := .4;
```

¹Maple V Release 3 for SGI. Copyright © Waterloo Maple Software.

```

R1 := 40000; A := 100; C := 1*10^(-10);
> g1 := evalf(gv)
> G := 20*log10(abs(g1))
>
>
-----
> plotsetup(ps, plotoutput='G1m.ps', plotoptions='portrait');
> plot3d(G, Delta=0..1, omega=1000..1000000000, axes=boxed,
title='Gain (dB) versus 2Pi*frequency (rad/sec) and Delta (m)');
>
>
-----
> G1 := subs(Delta=1.080,G)
-----
> #plotsetup(ps, plotoutput='gain-w.ps', plotoptions='portrait');
> plot({[log10(omega), G1, omega= 1000..1000000000]}, title='Link Gain
(dB) versus log10(w), Intensity Model');
> # Plot data points (in dB) with model
> ###100 := [4.80,-40]; 10 := [5.50,-40]; 11 := [6.50,-40];
12 := [6.80,-40]; 13 := [7.10,-40]; 14 := [7.28,-42];
15 := [7.40,-42]; 16 := [7.50,-42]; 17 := [7.70,-48];
18 := [7.80,-60]; 19 := [7.97,-70];
> #plotsetup(ps, plotoutput='gain-w-verity.ps', plotoptions='portrait');
> plot({[log10(omega), G1, omega= 1000..1000000000], [100, 10, 11, 12,
13, 14, 15, 16, 17, 18, 19]}, title='Link Gain (dB) versus log10(w),
Intensity Model and Experiment');
-----
> G2 := subs(omega=6000000, G)
-----
> #plotsetup(ps, plotoutput='gain-dl.ps', plotoptions='portrait');
> plot({[log10(Delta), G2, Delta= .01..100]}, title='Link Gain (dB)
versus log10(Delta), Intensity Model');
-----
>

```

E.2 Gain Analysis - Phase Model

Script file gain-feedback-alt.ms.

```

> ### Phase Gain Model: 1st order linear feedback analysis - EIA, JMR
> May '97
> restart
-----
> y := Po/2*(1 + cos(phi))

```

```

-----
> y1 := convert(taylor(y,phi=Pi/2,2),polynom)
-----
> G1 := -2*Pi*Delta*eta/(lambda[o]^2)
> G2 := -1/2*tff*R*Po*Z(s)
> G3 := B*Pi/V[Pi]
-----
> GAINo := (G1*G2)/(1 + G2*G3)
-----
> # Model parameters
> ##lambda[o] := 1.064*10^(-6); eta :=7.0*10^(-14); evalf(Pi); V[Pi]
> :=7.5; Po := .004; tff := 0.25; R := .4; R1 := 330; R2 := 330; B :=
> 100; C := 1*10^(-10);
-----
> GAIN := subs(Z(s) = -I/(C*omega),GAINo)
-----
> plot({[log10(omega), 20*log10(abs(subs(Delta=1.080,GAIN)))], omega=
> 1000..1000000000}], title='Link Gain (dB) versus log10(w), Phase
> Model')
>
> ## Plot Data with Model
> plotsetup(ps, plotoutput='alt-gain-w-verity.ps',
> plotoptions='portrait')
> ##100 := [4.80,-40]; 10 := [5.50,-40]; 11 := [6.50,-40]; 12 :=
> [6.80,-40]; 13 := [7.10,-40]; 14 := [7.28,-42]; 15 := [7.40,-42]; 16
> := [7.50,-42]; 17 := [7.70,-48]; 18 := [7.80,-60]; 19 := [7.97,-70];
>
> plot({[log10(omega), 20*log10(abs(subs(Delta=1.080,GAIN)))], omega=
> 1000..1000000000],[100, 10, 11, 12, 13, 14, 15, 16, 17, 18, 19]},
> title='Link Gain (dB) versus log10(w), Phase Model and Experiment')
-----
> plotsetup(ps, plotoutput='alt-gain-dl.ps', plotoptions='portrait')
> plot({[log10(Delta), 20*log10(abs(subs(omega=1000000,GAIN)))], Delta=
> .01..100}], title='Link Gain (dB) versus log10(Delta), Phase Model
> and Experiment')
-----
>
-----
>
>

```

E.3 Dynamic Range Analysis

Script file sfdrrl.ms.

```
> restart;
```

```

> readlib(log10)
-----
> # Spurious-Free Dynamic Range Model of FM Link
> # Jeffrey Roth
> VVoo := ((Ii*R*Z)/2)*(cos( (Pi*Vo*lambda[o] +
> 2*Pi*Delta*v[pi]))/(v[pi]*lambda[o]*(1 + eta*Vi/lambda[o])))
> # Assume feedback loop maintains Vo=Vpi/2 and wavelength deviation
> small, resulting in...
> VVo := R*Z*(Phi/2)*cos( Pi/2 +
> (2*Pi*Delta*v[pi]))/(v[pi]*lambda[o]*(1 + eta*Vi/lambda[o]))
-----
> p1 := Vo = convert(taylor(VVo, Vi, 4), polynom)
> pv1 := solve(p1, Vo)
>
> # Change of variables
> pv2 := subs(sin((2*Pi*Delta)/lambda[o]) = X,
> cos((2*Pi*Delta)/lambda[o]) = Y, pv1)
> pv3 := simplify("
> p3 := subs(cos((2*Pi*Delta)/(lambda[o] + eta*VI)) = P,
> sin((2*Pi*Delta)/(lambda[o] + eta*VI)) = Q, pv3)
> # Do trick to avoid expanding other sine/cosine terms
> Vi := nu*cos(omega1*t) + nu*cos(omega2*t)
> expandoff(P,Q,X,Y)
> p41 := expand(p3)
> p5 := combine(p41, trig)
>
> p6 := subs(cos(omega1*t) = Omega1, p5)
> F1o := coeff(p6, Omega1)
> evalf(subs(Delta=1.00, F1o))
> F1 := subs(X = sin((2*Pi*Delta)/lambda[o]), Y =
> cos((2*Pi*Delta)/lambda[o]), P = cos((2*Pi*Delta)/(lambda[o] +
> eta*VI)), Q = sin((2*Pi*Delta)/(lambda[o] + eta*VI)), F1o)
> p6 := subs(cos(omega2*t - 2*omega1*t) = Omega3, p5)
> F3o := coeff(p6, Omega3)
> F3 := subs(X = sin((2*Pi*Delta)/lambda[o]), Y =
> cos((2*Pi*Delta)/lambda[o]), P = cos((2*Pi*Delta)/(lambda[o] +
> eta*VI)), Q = sin((2*Pi*Delta)/(lambda[o] + eta*VI)), F3o)
> ## Noise Floor (g is voltage gain)
> NF := k*T + k*T*abs(g)^2 + 2*q*IDC*50
>
> ## some constants
> NF := subs(k = 1.381*10^(-23), T = 273, q = 1.6*10^(-19), NF)
> ## DC current of ~ .5mA
> NF := subs(IDC= .0005, NF)
> ## from Gain analysis: (see file gain-feedback-alt.ms)
> NF:= subs(g = -247328.8485*((sqrt(-1)*Pi*Delta)/(omega +
> .266667*10^(8)*sqrt(-1)*Pi)),NF)
> #note! noise floor is complex!

```

```

> # Use 1 kHz frequency
> guy := abs(subs(omega=6*10^6, NF))
> #plotsetup(ps, plotoutput='noise-floor-bode.ps',
> plotoptions='portrait');
> plot({[log10(Delta),10*log10(1000*abs(guy)),Delta=.01..1000]}),
> title='Noise Floor (dBm) of link', axes='framed')
> #loglogplot(abs(1/(Delta^2 + sqrt(-1)*Delta))^20, Delta=.01..10);
>
-----
> Z := 1/(omega*C)
> ###lambda[o] := 1.064*10^(-6); eta :=5.7*10^(-14);
evalf(Pi); v[pi] := 5; V0 := 2.5; VI := 0; Phi:= .001; R := .5;
> ###C := 1.3*10^(-9); omega := 10^3;
-----
> with(plots, loglogplot, logplot)
> evalf(10*log10(1000*abs(NF)))
> x := (solve(NF = F3^2/50, nu)[1])
> evalf(subs(Delta=1.0, x))
> plot({[log10(Delta), 10*log10(abs(x)), Delta= .001..100]}), title='x
> intercept');
> # solve for 1st order output
> y := subs(nu = x, F1)
> z_alogz := ((1000*abs(y)^2/50)/(abs(1000*NF)))^10
> z := 10*log10(1000*abs(y)^2/50) - 10*log10(abs(1000*NF))
> #####plot({[log10(Delta),z,Delta=.01..10]}), title='Noise Floor (dBm)
> of link', axes='framed');
> #plot(z, Delta= .1..1, title='SFDR of link', axes='framed');
> #?numapprox[minimax]
>
>
> ###l1 := [[ n, (subs(Delta=n*1.064*10^(-2), z))] $n=1..100];
> ###l2 := [[ n, (subs(Delta=n*1.064, z))] $n=1..100];
> #l3 := [[ n, (subs(Delta=n*1.064*10^(0), z))] $n=1..10];
>
> plot(l1, n=1..100, style=point,symbol=circle, title='.01064m - 1.064m');
> #plot(l2, n=1..100, style=point,symbol=circle, title='1.064m - 106.4m');
> #plot(l1 ,n=1..20,style=point,symbol=circle, title='1.064m - 106.4m');
> #l1 := concat(l2,l3);
> #plotsetup(ps,plotoutput='sfdr-lowrange.ps',plotoptions='portrait,
> noborder');
> #####plot(l1, n=1..100, style=point,symbol=circle, title='SFDR (1 Hz
> bw) over range .01064m - 1.064m');
> #plotsetup(ps,plotoutput='sfdr-highrange.ps',plotoptions='portrait,
> noborder');
> #####plot(l2, n=1..100, style=point,symbol=circle, title='SFDR (1 Hz
> bw) over range 1.064m - 106.4m');
> #convert to dBm
> XX := evalf(10*log10(1000*x^2/50))

```



```

-----
>
-----
> # Delta = 1 m
>
> dummy := 8.4
> ##Delta := 1.00;
-----
> x := (abs(solve(NF = F3^2/50, nu)[1]))
> #x := subs(Delta = 1,x);
> XX := evalf(10*log10(1000*x^2/50))
>
>
>
> plot({[10*log10(1000*nu^2/50),10*log10(1000*abs(F1)^2/50),nu=.00001..10],
> [10*log10(1000*nu^2/50),10*log10(1000*abs(F3)^2/50),nu=.00001..10],
> [10*log10(1000*nu^2/50),10*log10(1000*abs(NF)), nu=.00001..10], [XX,
> 10*log10(1000*nu^2/50), nu=.0000000001.. .2236]}),
> title='1st, 3rd, Noise Floor Outputs (dBm) APPROX Delta 1 m');
-----
>
-----
>
>
>
> plotsetup(ps,plotoutput='noise-floor-bode.ps',plotoptions='portrait,
> noborder');
-----
>
-----
>

```

E.4 Noise Figure Analysis

Script file `nf.ms`. insert here.

```

> ## Noise Figure Analysis - Jeffrey Roth
> restart
>
> # Start out with noise floor, call it Nout: assume shot noise,
> thermal noise, and amplified thermal noise
> Nout := k*T + k*T*abs(gv)^2 + 2*q*IDC*50
> # Make a plot of Noise Floor
> # gain gvmod taken from gain-feedback-alt.ms
> gvmod :=-I*tff*R*Ii*Pi*(Delta)/lambda[o]^2*
> eta/omega/C/(1+1/2*I*tff*R*100*Ii*Pi/v[pi]/omega/C)
> nfloor := subs(gv = gvmod,Nout)
>

```

```

> noisefloor1Mhz := subs((k = 1.381*10^(-23), T = 273, q =
> 1.6*10^(-19), IDC = .0005, lambda[o] = 1.06421*10^(-6), eta
> =5.7*10^(-14), v[pi] = 5, Vo = 2.5, Ii = .004, tff = 0.5, R = .4,
> Rin = 10000, C = 100*10^(-12), omega = 6000000),nfloor)
> #plotsetup(ps,plotoutput='noise-floor-bode.ps',plotoptions =
> 'portrait, noborder')
> plot({[log10(Delta),
> 10*log10(abs(1000*noisefloor1Mhz)),Delta=.01..1000]}, title='Noise
> Floor (dBm) of link', axes='framed')
> # Input noise is just thermal noise
> Nin := k*T
>
> # Noise Figure
> ##NF := SNRin/SNRout = Nout/(Nin*g)
> NF0:= Nout/(Nin*abs(gv)^2)
>
> # Use voltage gain previously derived (see file gain.ms)
> NF := subs(gv = gvmod,NF0)
>
> NF1 := subs((k = 1.381*10^(-23), T = 273, q = 1.6*10^(-19), IDC =
> .0005, lambda[o] = 1.06421*10^(-6), eta =5.7*10^(-14), v[pi] = 5, Vo
> = 2.5, Ii = .004, tff = 0.5, R = .4, Rin = 10000, C = 100*10^(-12)),
> NF)
> # Look at 1 MHz;
> NF1Mhz := subs(omega=6000000, NF1)
> #plotsetup(ps,plotoutput='nf-bode-adjusted.ps',plotoptions =
> 'portrait, noborder');
> plot({[log10(Delta), 10*log10(abs(NF1Mhz)),Delta=.01..1000]},
> title='Adjusted Noise Figure (dB) of link at 1 MHz', axes='framed')
-----
>
-----
>
> # This equation was taken out of Charlie's paper -
> # just checking it against mine for validity
> chc := 2 + q*Rin*R*tff*Ii/(k*T*gv)
> chc := subs(gv = gvmod, chc)
-----
> chc := subs((k = 1.381*10^(-23), T = 273, q = 1.6*10^(-19), IDC =
> .0005, lambda[o] = 1.06421*10^(-6), eta =5.7*10^(-14), v[pi] = 5, Vo
> = 2.5, Ii = .004, tff = 0.5, R = .4, Rin = 10000, C = 100*10^(-12)),
> chc)
-----
> chc1mhz := subs(omega=6000000, chc)
-----
> #plotsetup(ps,plotoutput='noise-figure-bode-charlie.ps',plotoptions
> = 'portrait, noborder');
> ###plot({[log10(Delta),

```

```
> 10*log10(abs(chc1mhz)),Delta=.01..1000],[log10(Delta),  
> 10*log10(abs(NF1Mhz)),Delta=.01..1000}], title='Noise Figure II (dB)  
> of link', axes='framed');\
```

Appendix F

List of Abbreviations

DPSSL	diode-pumped solid-state laser
EO	electro-optical
FM	frequency modulation
FMDD	frequency modulation with direct detection
FSR	free-spectral range
IMDD	intensity modulation with direct detection
MZI	Mach-Zehnder interferometer
Nd:YAG	neodymium-doped yttrium aluminum garnet
NF	noise figure
OPLL	optical phase locked loop
PBS	polarizing beamsplitter
PM	polarization maintaining
QWP	quarter-wave plate
RIN	relative intensity noise
SFDR	spurious-free dynamic range
SM	single mode
SNR	signal to noise ratio
WDM	wavelength division multiplexing
YBBM	Y-fed balanced-bridge modulator

References

- [1] W. C. Marra, J. Schesser, "Africa ONE: The Africa Optical Network," *IEEE Communications Magazine*, pp. 50-57, February 1996.
- [2] C. H. Cox, G. E. Betts, L. M. Johnson, "An Analytic and Experimental Comparison of Direct and External Modulation in Analog Fiber-Optic Links," *IEEE Transactions on Microwave Theory and Techniques*, Vol. 38, No. 5, pp. 501-509, May 1990.
- [3] H. G. Danielmeyer, F. W. Ostermayer, "Diode-Pump-Modulated Nd:YAG Laser," *Journal of Applied Physics*, Vol. 43, No. 6, pp. 2911-2913, June 1972.
- [4] D. D. Yang, P. Boucaid, F. H. Julien, L. Chusseau, J.-M. Lourtioz, "Laser Diode Modulation of 10.6 μm Radiation in GaAs/AlGaAs Quantum Wells," *Electronics Letters*, Vol. 26, No. 18, pp. 1531-1533, August 1990.
- [5] C. C. Teng, "Traveling-wave polymeric optical intensity modulator with more than 40 GHz of 3-dB electrical bandwidth." *Applied Physics Letters*, Vol. 60, No. 13, pp. 1538-1540, 30 March 1992.
- [6] E. R. Hedin, F. J. Goetz, "Experimental studies of electro-optic polymer modulators and waveguides," *Applied Optics*, Vol. 34, No. 9, pp. 1554-1561, 20 March 1995.
- [7] G. Lengyel, K. W. Jelley, R. W. H. Engelmann, "A Semi-Empirical Model for Electroabsorption in GaAs/AlGaAs Multiple Quantum Well Modulator Structures," *IEEE Journal of Quantum Electronics*, Vol. 26, No. 2, pp. 296-304, February 1990.
- [8] J. J. Zayhowski, J. A. Keszenheimer, "Frequency tuning of microchip lasers using pump-power modulation," *IEEE Journal of Quantum Electronics*, Vol. 28, pp. 578-580, 1991.

- [9] J. J. Zayhowski, A. Mooradian, "Frequency-modulated Nd:YAG microchip lasers," *Optics Letters*, Vol. 14, pp. 618-620, 1989.
- [10] A. Owyong, P. Esherick, "Stress-induced tuning of a diode-laser-excited monolithic Nd:YAG laser," *Optics Letters*, Vol. 12, pp. 999-1001, 1987.
- [11] J. J. Zayhowski, P. A. Schulz, C. Dill III, S. R. Henion, "Diode-pumped composite-cavity electro-optically tuned microchip laser," *IEEE Photonics Technology Letters*, Vol. 5, No. 10, pp. 1153-1155, October 1993.
- [12] P. A. Schulz, "Fast Electro-Optic Wavelength Selection and Frequency Modulation in Solid State Lasers," *The Lincoln Laboratory Journal*, Vol. 3, No. 3, pp. 463-478, 1990.
- [13] S. Yamamoto, N. Edagawa, H. Taga, Y. Yoshida, H. Wakabayashi, "Analysis of Laser Phase Noise to Intensity Noise Conversion by Chromatic Dispersion in Intensity Modulation and Direct Detection Optical Fiber Transmission," *Journal of Lightwave Technology*, Vol 8, No. 11, pp. 1716-1722, November 1990.
- [14] R. F. Kalman, J. C. Fan, L. G. Kazovsky, "Dynamic Range of Coherent Analog Fiber-Optic Links," *Journal of Lightwave Technology*, Vol. 12, No. 7, pp. 1263-1277, July 1994.
- [15] C. Cox, E. Ackerman, G. Betts, "Relationship between gain and noise figure of an analog optical link," *1996 IEEE Microwave Theory Technology Symposium Digest*, pp. 1551-1554, 1996.
- [16] R. Gross, R. Olshansky, M. Schmidt, "Coherent FM-SCM system using DFB lasers and a phase noise cancellation circuit," *IEEE Photonics Technology Letters*, Vol. 2, No. 1, pp. 66-68, January 1990.
- [17] J. Salzman, A. Katzir, "Heterodyne detection SNR: calculations with matrix formalism," *Applied Optics*, Vol. 23, No. 7, pp. 1066-1074, April 1984.
- [18] M. Kouroggi, C. H. Shin, M. Ohtsu, "A 134 MHz Bandwidth Homodyne Optical Phase-Locked-Loop of Semiconductor Diodes," *IEEE Photonics Technology Letters*, Vol. 3, No. 3, pp. 270-272, March 1991.

- [19] R. T. Ramos, P. Gallion, D. Erasme, A. J. Seeds, A. Bordonalli, "Optical injection locking and phase-lock loop combined systems," *Optics Letters*, Vol. 19, No. 1, pp. 4-6, January 1, 1994.
- [20] D. J. M. Sabido IX, T. K. Fong, R. F. Kalman, L. G. Kazovsky, "Linewidth-Insensitive Coherent Optical Analog Links," *SPIE*, Vol. 1703, pp. 504-522, 1992.
- [21] R. T. Ramos, A. J. Seeds, "Comparison between first-order and second-order optical phase-lock loops," *IEEE Microwave and Guided Wave Letters*, Vol. 4, No. 1, pp. 6-8, January 1994.
- [22] W. R. Cook, H. Jaffe, "Electrooptic Coefficients," *Landolt-Bornstein, New Series*, Vol III/11, Springer-Berlag, New York, 1979.
- [23] R. C. Alferness, "Waveguide Electro-Optic Modulators," *IEEE Transactions on Microwave Theory and Techniques*, Vol. MTT-30, No. 8, pp. 1121-1137, August 1992.
- [24] G. L. Abbas, V. W. S. Chan, T. K. Yee, "A dual-detector optical heterodyne receiver for local oscillator noise suppression," *Journal of Lightwave Technology*, Vol. LT-3, No. 5, pp.1110-1122, 1987.
- [25] E. L. Wooten, R. L. Stone, E. W. Miles, E. M. Bradley, "Rapidly Tunable Narrowband Wavelength Filters Using LiNbO₃ Unbalanced Mach-Zehnder Interferometers," *Journal of Lightwave Technology*, Vol. 14, No. 11, pp. 2530-2536, November 1996.
- [26] C. H. Cox III, "Gain and noise figure in analogue fibre-optic links," *IEE Proceedings-J*, Vol. 139, No. 4, August 1992.
- [27] T. Y. Fan, Electro-optically tuned microchip lasers, (Personal conversation).
- [28] N. MacKinnon, C. J. Norrie, B. D. Sinclair, "Laser-diode-pumped, electro-optically tunable Nd:MgO:LiNbO₃ microchip laser," *Journal of the Optical Society of America B*, Vol. 11, No. 3, pp. 519-522, March 1994.
- [29] "Sub-Hz linewidth Nd:YAG stabilized lasers," *NuFocus Technical Notes*.
- [30] Optical Spectrum Analysis, Hewlett-Packard Application Note 1550-4 "Optical Spectrum Analysis Basics", Hewlett-Packard Company, Rohnert Park, CA, 1996.

- [31] *Waves and Fields in Optoelectronics*, Hermann A. Haus, Prentice-Hall, Engelwood Cliffs, New Jersey, 1984.